Li leaching from Li carbonate-primer

Transport pathway development from the scribe edge of a primer/topcoat system

Visser, P.; Ranade, S.; Laird, J. S.; Glenn, A. M.; Hughes, A. E.; Terryn, H.; Mol, J. M.C.

Important note
To cite this publication, please use the final published version (if applicable).
Please check the document version above.

Li leaching from Li carbonate-primer: Transport pathway development from the scribe edge of a primer/topcoat system

P. Visser [a,b], S. Ranade [c], J.S. Laird [d], A.M. Glenn [e], A.E. Hughes [e,f,*], H. Terryn [a,g], J.M.C. Mol [a]

[a] *Department of Materials Science and Engineering, Delft University of Technology, Mekelweg 2, 2628 CD, Delft, the Netherlands*
[b] *AkzoNobel, Rijksstraatweg 31, 2171 AJ, Sassenheim, the Netherlands*
[c] *Department of Metallurgical and Materials Engineering, Indian Institute of Technology Madras, Chennai, Tamil Nadu, 600036, India*
[d] *School of Chemistry, University of Melbourne, Melbourne, 3000, Australia*
[e] *CSIRO Minerals Resources, Clayton, Victoria, 3169, Australia*
[f] *Institute for Frontier Materials, Deakin University, Burwood, Victoria, Australia*
[g] *Department of Materials and Chemistry, Research Group Electrochemical and Surface Engineering, Vrije Universiteit Brussel, Pleinlaan 2, 1050, Brussels, Belgium*

ABSTRACT

Depletion depths of inorganic components from a scribe edge in a polyurethane primer containing Li_2CO_3, MgO, $BaSO_4$ and TiO_2 beneath a topcoat, were determined using a range of techniques including SEM/EDS and proton induced X-ray and γ-ray emission spectroscopies. SEM of sections cut using an ion beam revealed scribe damage penetrating 20–25 μm away from the scribe edge prior to leaching. After neutral salt spray (NSS) exposure a leached zone developing from the scribe edge was observed. For longer NSS exposure times (>96 h) this leached zone of nearly complete Li and Mg depletion did not develop any deeper than the scribe damaged region indicating that the depletion zone was caused by mechanical damage due to scribing. At short times small voids were formed in Li_2CO_3 particles within the primer well away from the scribe (100–260 μm) whereas a mixture of void and detachment in and around Li_2CO_3 particles was observed at longer times. The detachment was assumed to be part of a channel network within clusters of particles. Internal stresses within the primer resulting from buildup of inhibitor dissolution product within the voids were modelled using finite element analysis. It was found that strains related to von Mises stresses were concentrated around the inorganic particles and developed preferentially within the plane of the primer beneath the topcoat with some indication of concentration towards the primer/metal interface. These stresses resulted from osmosis and swelling related to the voids. They were also attributed to the observed cracking of the binder at some locations. Leaching experiments showed that Li was released very rapidly from the primer. The leaching data was modelled using a power law where the mass released is proportional to t^n where the n is an index that reflects the kinetic behavior dictated by the evolving primer porosity. In this study n values between 0 and 1 were observed for all species, with Li starting at around 0.7 but rapidly decreasing to close to zero.

1. Introduction

The search for alternatives to chromate-based inhibitors in the aerospace industry, particularly for high strength Al-alloys is still an active area of research [1–3]. One class of inhibitors that has seen some intense interest in recent years is the Li-based inhibitors that have been reported by Visser and co-workers [4–10]. A recent paper has shown that Li-containing compounds provide good protection to aluminium alloys through the spontaneous formation of coatings based on *pseudo*-boehmite (*p*-B) and a particular layered double hydroxide (LDH)

often referred to as hydrotalcite [4]. Hydrotalcites have been shown to provide very good corrosion protection for aluminium alloys [11–21] and their ion exchange capabilities, particularly carbonate for chloride, have been the basis of a proposed self-healing mechanism for these coatings [22–26]. Boehmite and *p*-B coatings also demonstrate some protective properties against corrosion [27,28] but would probably be considered less effective than LDH coatings even though some good performance has been reported [29].

In an earlier paper by the authors [30] it was found that Li release into solution from a Li_2CO_3-containing primer without topcoat, was

---

complex. The primer was a fully formulated polyurethane (PU) primer system containing the pigment TiO_2 and extenders MgO, $BaSO_4$ in addition to the Li_2CO_3 -inhibitor. Initially there was rapid release of Li (between 5–10 h) from the coating matrix, but after longer exposure times (> 24 h) the Li release was reduced to very low levels. Following the initial, high level of Li release, Mg and, to a lesser extent Ba, were also released. It was concluded that the complex release was related to the ongoing development of a network of transport paths (longer diffusion paths and increased volume) with increased immersion time. The *generation* of these transport paths could be classified into two categories including (i) *chemical* where dissolution at the interface of particles created local voids which eventually became connected to form channels and (ii) *mechanical* where it was proposed that internal stresses, perhaps created by swelling due to hydration of inorganic particles as well as osmotic pressure, resulted in local mechanical failure of the PU binder resulting in void and, subsequently, network formation. In the mechanical case these conclusions were supported by finite element analyses using observed inorganic particle distributions. While dissolution occurred around Li_2CO_3 particles it was not confined to these particles with all the other phases being involved in creating an internal channel network through which the dissolution product (an electrolyte potentially containing some or all of Li^+, Mg^{2+}, Ba^{2+}, CO_3^{2-}, SO_4^{2-} OH^-) could be leached as well as the *external* electrolyte (Na^+, Cl^-) could penetrate the primer. An additional factor which was considered was the timescales for water molecules to enter the primer which can be up to two orders of magnitude faster than ions from the external electrolyte in polymer systems [31–34]. Water-uptake occurs rapidly in primer formulations [35]. It can be separated from uptake of the *external* electrolyte by days. This means that in the earliest stages of immersion, hydration and dissolution reactions, can occur on the surface of inorganic particles [35]. This is because the binder adjacent to inorganic particles will be saturated with water but, like ions from the *external electrolyte*, ions from the *internal electrolyte* cannot diffuse into the binder at this early stage of immersion because the free volume of the PU is smaller than the ion sizes [30]. Similar conclusions have been reached for epoxy systems [36–39]. Two effects result from this water-uptake. First, an osmotic effect is created due to water being drawn into the electrolyte developing at the particle/binder interface in an effort to "dilute" it. This effect is similar to deswelling in membrane science [31]. Second, the development of the *internal* electrolyte itself may cause internal stresses on the binder, particularly locally at the inorganic/binder interface which may spread further into the binder with time. The combination of these effects leads to internal stresses in the coating. These were previously proposed to cause some mechanical degradation of the coating.

Thus, the picture that emerged from our and others work was that, during the early stages of immersion, leaching occurred from particles directly exposed to solution. These may be individual particles or particles that were part of a larger cluster. With increased time leaching only occurs from particles that are incorporated into a cluster. Thus, ions from the *internal* electrolyte, created from dissolution of particles further away from the leaching interface, could only enter the *external* electrolyte through a network of channels created by partial/complete dissolution of connected particles perhaps facilitated by mechanical rupture of the PU. This is the model based on leaching through particles clusters [30,36,37,40,41]. The authors earliest work studied an epoxy primer where $SrCrO_4$ was the only component, so only $SrCrO_4$ particle clusters were observed [40]. Latter studies showed that where there are more than one inorganic particle type then all the different types of particles can be involved in network formation [30,36,42].

In a previous study by the authors, leaching from the as-applied surface of a fully formulated Li_2CO_3-inhibited primer was examined. In that study it was demonstrated that as immersion time increases, a network of voids and channels for leaching develops. Initially, this is confined to Li_2CO_3 particles and clusters, but, after longer times, can develop around other types of inorganic particles as a result of internal

stresses due to dissolution reactions at the interface of those particles and the binder. This means that the composition of the *internal* electrolyte may change depending on the chemistry of other inorganic particles. In this study, the leaching into a scribe from the cut edge of a primer under a topcoat is examined in detail. There are several studies of protection within a scribe resulting in leaching of an inhibitor from a primer both for this Li_2CO_3-based coating system [4,5,7,9], as well as other inhibited systems [43–48]. However, much less has been done to characterize inhibitor depletion at the cut edge of the Li_2CO_3-based primer systems [49]. Therefore, the particular focus of this paper is on tracking changes that occur from the cut edge of the primer beneath a topcoat during the leaching process. Specifically, the leaching of Li and Mg is followed using proton induced X-ray and γ-ray emission spectroscopies (PIXE and PIGE respectively) as well as scanning electron microscopy in combination with energy dispersive X-ray spectrometry (SEM/EDS). Leaching from the cut edge presents one considerable geometric difference to leaching from the as-painted surface of the primer in that leaching can only occur for clusters that form a network connected to the cut edge. So, the volume of inhibitor released is limited to the cluster size distribution along the scribe edge. Second, the accumulation of product (*e.g.* corrosion product, precipitated leachate) on the cut edge will considerably modify leach rates. Thus, it can be anticipated that the leaching profile with leach time will be complex as shown below.

2. Experimental

2.1. Materials and sample preparation

The primer (coating) was a high solids formulation based on a PU resin with a polyisocyanate crosslinker and formulated to a pigment volume concentration of 30 % as described elsewhere [10]. The inorganic pigments included Li_2CO_3-inhibitor, MgO and $BaSO_4$ fillers and TiO_2 as pigment. Trace element analyses of the various inorganic components of the paint indicated that the $BaSO_4$ contained 0.9 %m/m Sr, and small amounts of Si, Ca, Al and Ti. The MgO contained 1500−1900 ppm by weight of Ca, 400−700 ppm by weight K and lesser amounts of other elements (Table 1). The Li_2CO_3 contained alkali metals (Na, K) in the range 400–800 ppm by weight. Particle size distributions for these additives were determined by dispersing in a solvent which was methylethylketone for Mg-hydroxide, TiO_2 and Li_2CO_3, where water was used for the $BaSO_4$. The $BaSO_4$ particles had the largest particles (up to 50 μm) and the largest spread in particles size. The TiO_2 particles were the smallest (up to 14 μm) and slightly smaller than the MgO. The Li_2CO_3 particle size distribution ranged up to 18 μm.

The top coat used in this study is based on the same polyurethane high solids formulation as the primer but without the incorporation of the pigments and extender.

AA2024-T3 was used as a substrate for coating, typical breakdown for this alloy is reported elsewhere [50]. The AA2024-T3 was prepared

Table 1
Chemical Composition of inorganic additives used in this study.

	Li_2CO_3 mg/kg	TiO_2 %m/m	MgO mg/kg	$BaSO_4$ %m/m
Al	5	1.4	70−77	0.1
Ca	91−98	–	1500−1900	0.1
Na	660−810	–	180−210	0.4
Ba	2	–	2−5	res
Si	–	–	–	0.4
Sr	–	–	–	0.9
Ti	–	–	–	0.1
Zr	–	0.4	–	–
Fe	2	–	73−78	–
Mn	–	–	13−15	–
Ni	–	–	5−6	–
K	400−700	–	200−300	–
Mg	39−40	–	–	1

by standard anodising according to aerospace requirements (AIPI 02-01-003) at Premium AEROTEC, Bremen Germany. This included the following steps; degrease, alkaline clean, acid desmutting followed by anodising in tartaric-sulphuric acid to produce a 2−3 μm thick oxide layer. Subsequently, the primer was applied by spraying using a high volume low pressure (HVLP) spray gun in a single pass to achieve a dry film thickness of approximately 30 μm, in practice the coating was typically 30–40 μm. The primer was cured for 16 h at 23 °C / 55 % RH before the topcoat layer was applied in a similar fashion as the primer to achieve a layer thickness of around 20 μm. After this, the total coating system was cured for 16 h at 23 °C / 55 % RH followed by a 30 min baking cycle at 80 °C.

For the leach-rate determination, coated samples with a surface area of 28 cm^2 were immersed in 50 mL deionized water. To ensure sufficient leaching from the cut edges of the coating, the coatings were damaged with twenty parallel cuts with a length of 5 cm penetrating the coating down to the substrate using a scalpel. This resulted in a total scribe length of 1 m before the immersion. Samples were taken and the solution was replaced with fresh demineralized water after regular intervals from 5 min up to 192 h immersion. The samples were acidified with nitric acid to a concentration of 0.1 M and analysed with inductively coupled plasma atomic emission spectroscopy (Arcos NT ICP-AES) using scandium as an internal standard. All measurements for the leaching curves were executed in duplicate.

Before exposure to the neutral salt spray (NSS), the primer-topcoat samples were scribed from corner to corner using a mechanical milling device leaving a U-shaped artificial damage of 1 mm wide and 100 μm deep into the metal substrate. The panels were exposed for times up to 500 h in a test chamber operated according to ASTM B117.

2.2. Scanning electron microscopy and energy dispersive X-ray spectroscopy (SEM/EDS)

The SEM analysis was divided into two sections, each looking at different aspects of the primer/topcoat system, and consequently each requiring different approaches to sample preparation. In the first section, a traditional SEM characterisation was conducted on a cross-section of the sample to look at morphology as well as inhibitor particle and elemental distribution within the primer layer. Consequently, traditional, metallographic cross-sectional samples were prepared for these analyses. To this end, samples were first cut with a hack saw and oriented such that the scribe was perpendicular to the plane of polish. They were then mounted in thermosetting phenolic resin (conductive bakelite) for high edge retention of the paint layer and, after setting were ground with SiC papers in the sequence 300, 600, 1200 and 2000 grit. After grinding, samples were polished with diamond abrasive in the sequence 8, 3, 1 and 0.25 μm. At all stages of the grinding and polishing, samples were either dry ground, or lubricated with non-aqueous lubricants to avoid unintended dissolution of inhibitor or other particles. Samples were then carbon coated to a thickness of approximately 15 nm for SEM examination which was carried out in a FEI Quanta 400, field emission, environmental SEM. Basic secondary and backscattered electron imaging was conducted using a beam energy of 10 kV and probe current of approximately 0.15 nA. These conditions were found not to damage the relatively sensitive polymer binder in the primer layer. EDS mapping was carried out using a Bruker e-Flash EDS detector and post processed using Bruker Esprit software. Mapping, conditions of 10 kV and 1.1 nA were used to obtain a high enough count rate for reasonable map statistics. Mapping was conducted overnight for approximately 13.3 h.

For the second section of the SEM analysis, the authors investigated the formation of particle clusters and channel networks within the primer which facilitate leaching of the inhibitor. Furthermore, the authors decided to examine the extent to which machining of the scribe introduces mechanical damage to the primer and its adherence to the substrate. For this part of the investigation ion beam slope cutting (IBSC)

was selected as the sample preparation method of choice since this method, although sectioning a much smaller area of sample than the traditional metallographic method, imparts no mechanical damage as adjudged from sections of the coating without NSS exposure and virtually no chemical damage whatsoever to the sample and therefore could not cause any ambiguity in interpreting the SEM results. Ion beam sectioning is emerging as a useful technique for sectioning coatings [51]. The instrument used for slope cutting was a Technoorg Linda SC2000 argon, ion beam polisher and slope cutter.

Using this technique, the sample preparation began with a small sample of the painted and scribed aluminium, measuring approximately 10 mm × 10 mm which was given a preliminary grind on 1200 grit SiC paper with no lubrication. The sample was then mounted on a backing plate with conductive carbon paint and inserted into the sample holder ready for slope cutting. The slope cutting sample holder positions the sample at an angle 30° downwards from the line of the ion beam (i.e., 30° downwards from horizontal) producing a newly cut surface at an angle of 30° to the plane of the topcoat. The sample was carefully aligned behind a titanium mask using a binocular microscope so that the scribe was perpendicular to the edge of the newly cut surface. For the slope cutting, a beam energy of 10 kV was used for approximately 4 h, and the sample was oscillated back and forth to an angle of ±40° from the line of the ion beam, which remains stationary during cutting. This arrangement is shown schematically in Fig. 1, where the cross-hatched area is the new surface cut by the ion beam.

After sectioning was complete, the sample was taken out of the ion beam slope cutter, and then removed from the sample holder. The sample was then mounted on a 30 °SEM stub so that the newly cut surface would be perpendicular to the electron beam in the SEM. The sample was then coated with a 6 nm film of conductive carbon in a Leica EM ACE 600 carbon coater. SEM examination was conducted in the same SEM as that used for the first section of the analysis, however a beam energy of 5 kV was used for the imaging instead of 10 kV to further reduce the beam damage imparted to the sample by the electron beam.

2.3. Proton-induced X- and ɣ-ray emission (PIXE/PIGE)

PIXE and PIGE have been described in detail previously [49,52]. 3 MeV protons were focused on the sample to approximately 2 μm using a separated quintuplet lens designed for optimal balance between high spatial resolution and maximum beam current. Beam currents were typically in the 0.5−1 nA range. A large area Ge(Li) ɣ-ray detector was placed approximately 5 mm directly behind the sample for a maximum acceptance solid angle. A LiF crystal and pure Al were used for the calibration of the ɣ-ray detector energy axis. For PIXE, the 100 mm^2 Ge (Li) detector was mounted at 45° to the incident proton beam and 3–4 mm from the sample. A 100 μm thick pure Al filter was placed in front of the detector to reduce overall X-ray intensity. Scan areas chosen for analysis varied, but generally ranged from 10 to 50 μm x 200 μm. The analysis depth was approximately 10–20 μm for both methods. For data collection the sample was moved in a grid of points under the proton beam. At each point PIGE and PIXE spectra were collected for each pixel thus forming a hyperspectral data set.

After collection, further data analysis was performed using GeoPIXE [53] where regions of interest (ROI) such as the primer, aluminium alloy or depletion zones were examined in more detail by extracting spectra from each of these ROIs. Both the Li 429 and 479 keV lines were used for PIGE; the 429 keV peak has the greatest surface sensitivity but is less intense [54]. The presence of these unambiguous Li peaks makes PIGE an excellent technique for following changes in the Li distribution since Li only comes from the inhibitor particles in the primer in this study [55]. In PIXE the signature K and L-series X-ray emission lines were used for element identification.
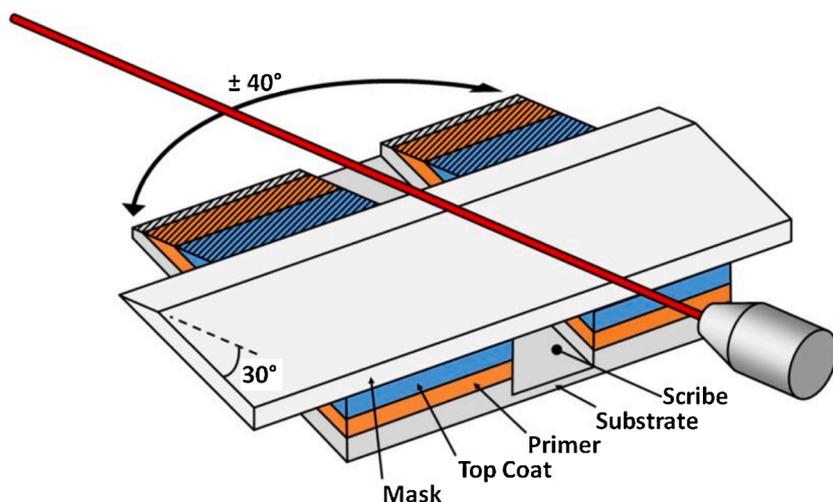
Fig. 1. Schematic representation of the ion beam slope cutting arrangement used for the "particle cluster and channel network formation" part of the investigation. The painted sample is positioned behind a titanium mask at a downward angle of 30° from the line of an argon ion beam. After careful alignment, the sample is oscillated back and forth under the ion beam and the new surface (cross-hatched in the schematic) is cut by the argon ions. This surface is virtually free of mechanical or chemical damage.

2.4. Finite element analysis

To simulate the influence of internal stresses, finite element analysis (FEA) was adopted in an attempt to trace the resultant elastic and shear strain distributions. The ANSYS Student version 2020 R1 is a software package that enables the modelling of mechanical behaviour of materials in various modes such as with tensile, compressive and bending loads. It is possible to create and view the models in two as well as three dimensions. The software comes with a library of materials (non-metallic, metallic, gaseous, magnetic, etc.) with their chemical and physical properties. The module "Static Structural" was used to simulate the coating, and the fillers. All the connections between fillers, coating layers, and substrate were set to "Bonded". The smoothing option was adjusted to "medium" and the transition to "fast", along with the span angle centre kept at "fine". The posterior side, far end of the model (away from the fillers), and the bottom of the length of the structure was constricted using the "Fixed support" option. Two pressures (0.01 MPa and 10 MPa) were applied to one of the faces of three of the voids in the model in a direction normal to the face. This pressure range used in the modelling spans a likely range of internal pressures in the coating. The results of the analysis have been presented in the form of strain calculated according to the von Mises yield criterion [56]. This criterion provides that yielding will occur when the octahedral shear stress calculated from the 3 principal stresses exceeds the shear yield stress of the material. The strains reported are calculated based on the result of the applied stress level and are defined as $\Delta l/L$ where Δl is the deformation and L is a characteristic length of the system. Normally Δl is very small leading to very small levels of strain. Clearly as the applied stress increases the level of strain also increases. The material properties used for the fillers and the coatings were typical and selected from the standard data available in the software library. While PU foam (rigid) and PU foam (flexible) were chosen as the respective materials for the primer and topcoat, the fillers were given properties of titanium alloy, magnesium alloy, structural steel, and aluminium alloy. The material for substrate was set to a high strength wrought aluminium.

3. Results

The results section begins with characterization of the primer in cross-section prior to and after various times of exposure to NSS. SEM/EDS, PIGE and PIXE have been used to examine depletion that develops in the coating whereby coating components, particularly Li can be transported from the body of the primer to the external electrolyte in the scribe.

3.1. Characterisation of the scribed, un-leached primer

Scribing can produce different types of damage at the cut edge of the coating. Fig. 2 shows an IBSC cross-section through the topcoat and primer into the underlying AA2024-T3 capturing the different types of damage that can occur upon scribing. This cross-section shows considerable deformation within the AA2024-T3, primer and the topcoat. The level of scribe edge displacement of the base AA2024-T3 from the un-damaged region, i.e. deformation and burring, is indicated by the deviation of the vertical yellow arrows from the dashed yellow baseline. The same magnitude yellow arrows have been used to indicate the displacement at the primer/topcoat interface within the primer from the undamaged region. In the case of the primer the displacement is larger (difference between yellow arrow and the green dashed line at the primer/topcoat interface) indicating more deformation in the primer. The additional deformation is probably due to detachment around, and displacement of Li_2CO_3 (red arrows) and $BaSO_4$ (blue arrows) particles; these are the largest particles in the primer. The approximate damaged area boundary is indicated by the green dashed line) and varies from 20 μm to 50 μm. The anodised layer is also cracked and at one-point split (orange arrows). Fig. 2 is only one section through the scribe. Other sections showed different levels of deformation as can be seen in various micrographs throughout this manuscript. The presence of detachment around two of the inorganic particle types suggests that electrolyte ingress might be facilitated by the presence of a network of cracks caused by the scribing itself.

3.2. Characterisation of the scribed, leached primer

3.2.1. SEM/EDS

Fig. 3 (a) and (b) show typical secondary and backscattered electron images respectively of vertical sections through the primer and topcoat adjacent to the scribe edge after 500 h NSS exposure. The two coatings layers and the AA2024-T3 can be easily distinguished from one another through the presence of the TiO_2 and $BaSO_4$ particle types in the primer which are the whitest features seen in the backscattered electron image (Fig. 3(b)). The MgO and Li_2CO_3 particles have similar to and darker than greyscale, respectively, compared to the PU in which they are embedded, making them more difficult to see in this image. With respect to Fig. 2, some deformation can be seen in the topcoat (it thickens toward the scribe edge) but there is no apparent deformation at this scale in the AA2024-T3 or primer in this cross section. The backscatter image (Fig. 3(b)) highlights where an oxide layer has developed over parts of the cut edge of the primer and topcoat during leaching. Fig. 3(c) and (d) are backscattered electron images looking into the scribe (viewed at 15
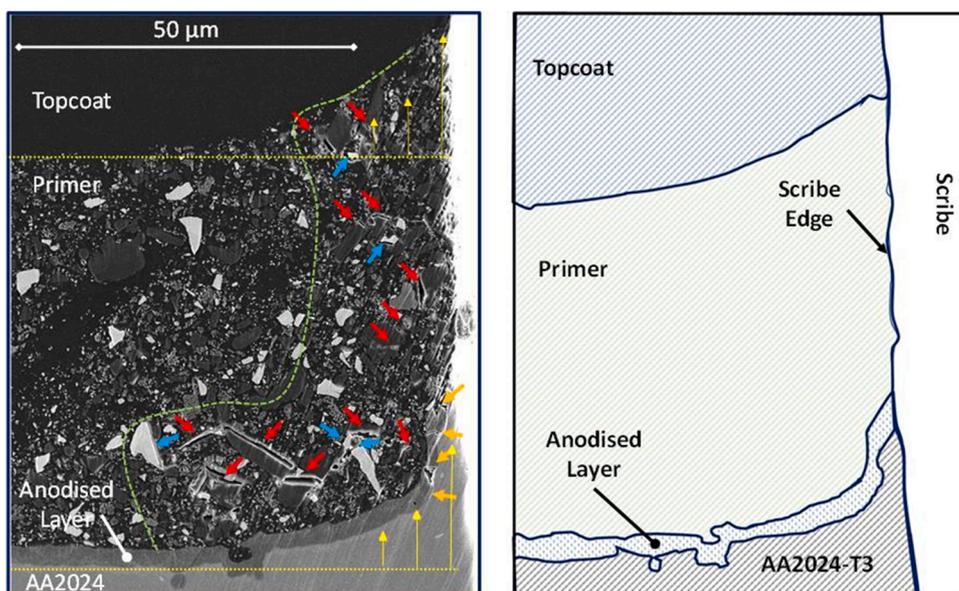
Fig. 2. Left - SEM image of deformation and damage at a section of scribe edge prior to any electrolyte exposure. Interfacial detachment has occurred at Li_2CO_3 particles (red arrows) and $BaSO_4$ particles (blue arrows). Orange arrows indicate cracking in the anodised layer. Yellow dashed lines indicate the baseline for the yellow arrows that show the level of deformation in the AA2024-T3. The green dashed line provides a rough indication of where damage has occurred. Right – Schematic of the image on the left including the position of the scribe edge and the scribe.

°C from the horizontal see Fig. 3(g)) where the cut edge of the coating system meets the AA2024-T3, both prior to ((c) and (e)) and after 8 h NSS ((d) and (f)). Evidence of burring can be seen at the primer/scribe interface Fig. 3(c) which is the same level of deformation as seen in the section in Fig. 2. Prior to NSS exposure it can be seen that scribing produces a ragged edge to the coating system and can result in fragments of paint within the scribe itself along with the deformation seen in Fig. 2. Similar observations have been reported for scribed $SrCrO_4$-inhibited epoxy primers [43]. Fig. 3(e) is an image of the interface between the topcoat and the primer. This interface is also ragged and some of the inorganic particles may be embedded into the topcoat. After exposure to NSS for 8 h (Fig. 3(d)), corrosion product is observed in the scribe in addition to the other features displayed in Fig. 3(c). Moreover, in addition to amorphous corrosion product, there are regions of either *p*-B or LDH as determined from appearance [4,7,8,57] (Fig. 3(f)). This occurs both on the polymeric interface as well as in the scribe itself. On the polymer interface, this corrosion product will act as a diffusion barrier.

After 500 h, the presence of Li in the scribe can be confirmed using the PIGE Li_{479} and Al_{1014} maps (Fig. 4 (a) and (b), respectively). In the Li map (Fig. 4 (a)) the highest intensity Li is shown in bright yellow and reveals the distribution of the Li_2CO_3 particles in the primer beneath the topcoat ((Fig. 4 (a) bottom)). The corresponding PIGE spectrum shows that there is significant Li in the coating (spectrum in Fig. 4 (c)). It also shows varying distribution of Li in the scribe (Fig. 4 (a)) with a small Li peak in the corresponding spectrum (Fig. 4 (c) blue arrow) from the scribe. Clearly both the Li and the Al intensities vary across the scribe surface indicating a range of Al/Li ratios but confirming that some Li reacts in the scribe presumably forming LDH.

Fig. 5(a)–(f) shows vertical sections through the coating system and metal after various exposure times to NSS including prior to exposure (0 h). In some cases the sections reveal significant deformation and burring as described in Figs. 2 and 3. Every section contained a range of inorganic particles with different sizes and backscatter contrast. There is also the anodized layer (mid-grey) between the primer and the metal. Bright particles in the AA2024-T3 are intermetallic particles (IMPs) which contain a range of alloying elements [58,59]. Prior to NSS exposure only the inorganic particles in the primer and metal burrs were observed at the scribe edge (Fig. 5 (a)). After NSS exposure oxides develop on the scribe edge and as seen in Fig. 3, and can form a continuous surface oxide from the top to the bottom of the primer edge after long enough exposure time to NSS. As described for Fig. 3 these oxide structures included both amorphous oxide and a porous structure that could be

either *p*-B or LDH [7,8].

Mixed colour elemental maps for O, Mg, Al, S, Cu, Ti and Ba, derived from EDS mapping of the sections shown in Fig. 5, are presented in Fig. 6. There are a range of particles with similar backscatter contrast to Fig. 5 for which the composition can be qualitatively identified in Fig. 6. The brightest particles in the BSE images in Fig. 5 are orange (mix of red and yellow) in Fig. 6 suggesting that they are $BaSO_4$. The MgO particles are purple (mix of red and blue) and the TiO_2, which are the small particles tend to be a light blue colour. The large red particles (arising from only an O contribution to the colour), are Li_2CO_3 particles as shown below using PIGE. The anodized layer is a red-brown colour which is also the colour of the oxide at the scribe edge (both primer and topcoat). The similarity in colour is due to compositional similarities, not structural similarities. It is typically 2–10 µm thick.

During the course of exposure to NSS, the soluble components of inhibitor and other inorganic compounds diffuse from within the primer into the electrolyte in the scribe. This means that the concentrations of various inorganic components in the primer diminish with time, with the greatest decrease expected near and at the interface of the primer with the scribe. It is not straightforward, however, to measure the depth of depletion since it does not move as a discrete boundary into the primer, where there is complete depletion behind the boundary and no depletion ahead of the boundary. Depletion occurs by gradual dissolution of particles and transport through channels meaning that depletion occurs simultaneously at different levels over a range of depths away from the scribe edge. Consequently, depletion is measured in several different ways in this paper as described in this and later sections.

For the SEM results, depletion depths can be estimated from the data in Fig. 6 in the following qualitative way. One method is to measure the width where there is complete or near-complete removal of inhibitor. So, in this case the depletion depth of the Li_2CO_3 particles is defined as the region where there are very few red particles (or they are completely absent). Examples of depletion zones are shown in Fig. 6(c) using a white dashed lines. The zone of depletion has a variable depth from top to bottom of the primer and is similar in depth to the region of mechanical damage suggesting that mechanical damage creates macroscopic channels in the primer allowing direct access to electrolyte. Complete depletion from the mechanically damaged region, however, does not take into account partial dissolution around particles further away from the scribe. Moreover, the amount of depletion in any of the EDS cross sections varies from the top to the bottom of the coating and from one cross-section to the next, meaning that the depletion depth
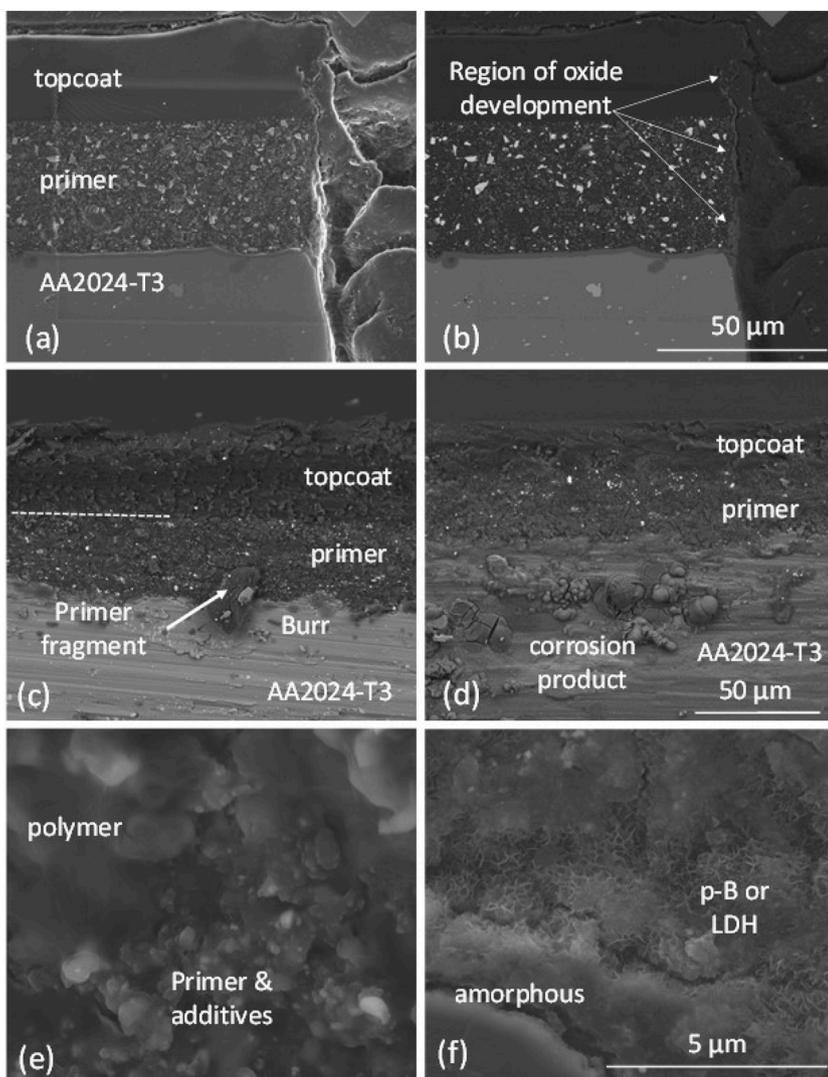
Fig. 3. (a) secondary and (b) backscattered electron images of the primer and topcoat after 500 h exposure to NSS. Oxide deposition on the cut edge of the coating (primer and topcoat) is highlighted by the white arrows in (b). (c) Looking at the cut edge of the primer prior to NSS exposure and (d) after 8 h NSS exposure. Note the primer fragment on the edge of the scribe. (e) Scribe edge prior to exposure at higher magnification than (c) and (f) scribe edge of 8 h sample at higher magnification than (d). (g) schematic of sample configuration for different images in (a) to (f).
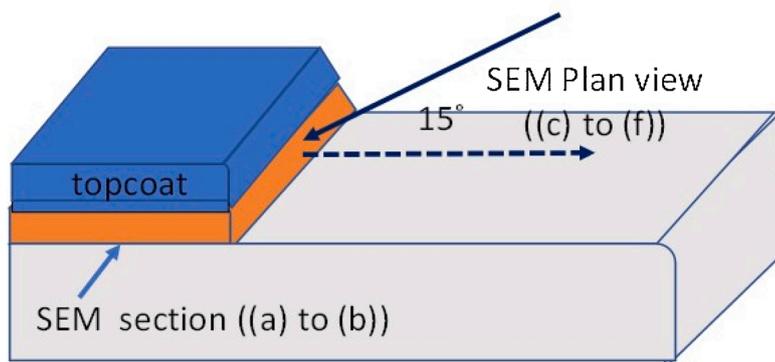
measured in this way can only be considered as indicative. Nevertheless, using this approach the depletion depths varied from 5 to 12 μms with the exception of the primer without exposure to NSS where there was a thin zone without any Li_2CO_3 particles which was around 2 μm. The origin of this Li_2CO_3 depleted zone is likely to be particle pull-out given the damage produced by scribing as seen in Fig. 2. Depletion depths determined in this fashion are reported in Fig. 7 and compared to other depletion depths whose derivation is described below. The figure also includes a hatched region indicative of the depth of mechanical damage created by scribing. Fig. 7 also includes detachment along interfaces of the PU with the Li_2CO_3 particles which is discussed below in the context

of network formation.

3.2.2. PIGE/PIXE

Fig. 8 shows 3-colour PIGE elemental maps of the same sections as in Figs. 5 and 6. Fig. 9 shows a mixture of PIGE and PIXE maps of the same sections as presented in Fig. 8. Fig. 8 is a 3-colour map containing Li (red features (Li 479 keV peak denoted Li_{479})), Al (blue (Al 1014 keV peak, denoted Al_{1014})) and Mg (green (1369 keV peak denoted Mg_{1369})) derived from the γ-ray emission. Fig. 9 is a 3-colour map containing Li (red (Li_{479})), Ba L series X-ray (blue) and Ti K-series X-ray (green). Thus, the combination of both figures contains information on all the
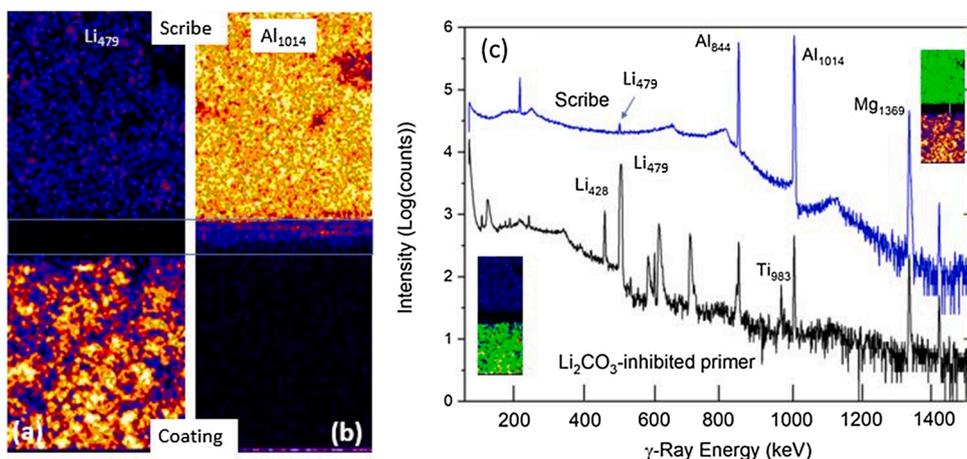
Fig. 4. PIGE results showing the presence of Li in the scribe after 500 h exposure to NSS. (a) Li map from the 479 KeV peak, (b) Al map from the 1014 keV peak and (c) respective spectra from the primer (under the topcoat) and the scribe. Bright green highlights where the spectrum was collected (either scribe or primer). The band between the two pale dashed lines in the centre of the maps indicates where there is an edge effect at the scribe. This is due to charge build-up in the coating (For interpretation of the references to colour in this figure legend, the reader is referred to the web version of this article.).

inorganics in the primer. The sampling depths of PIXE and PIGE are much deeper (≈ 20 μm) than that of SEM/EDS (< 2 μm at the beam energy used here). Consequently, the "apparent" areal density of particles is much higher for PIXE than for SEM/EDS. Thus, correlating features on a one-to-one basis is not so straightforward. Nevertheless, some correlation is possible with some "common" particles being identified between the two datasets. For example the white circle near the burr in the sample without NSS in Figs. 5(a), 6 (a), 8 (a) and 9 (a) encloses a dark particle in the backscattered electron image of Fig. 5(a), a bright red particle (indicating oxygen) in Fig. 6(a) and red areas in the Li_{479} maps in Figs. 8(a) and 9 (a), respectively. The PIGE spectrum from this particle (Fig. 10) shows a much higher signal of Li than the adjacent spectrum from the matrix which is also shown in Fig. 10. This type of correlation was performed on a number of particles thus demonstrating that the red features in the SEM/EDS analyses with only C and O contributions (probably CO_3^{2-}) can be unambiguously identified as Li_2CO_3 particles using the PIGE analysis.

The PIGE data in Fig. 8 shows a homogeneous mixture of the Li_2CO_3 and MgO particles in the body of the primer. Nearer to the scribe edge, the distribution of both these types of particles changes, showing depletion of Li with respect to Mg at 48 and 96 h, as well as overall reduction in the amount of Li in the 168 h and 500 h sections. Fig. 9 introduces the Ti information which is used here as a marker for the scribe edge position and more clearly reveals the depletion zones which are particularly prominent in the 48 h and 96 h data, but also evident to a lesser extent for 168 and 500 h. Note that the 48 and 96 h sample have more severe deformation at the scribe edge indicating that the depth of depletion is probably related to the degree of mechanical damage.

Depletion near the edge of the primer in the PIGE and PIXE maps could be determined in the same way as for the SEM/EDS. In this section however, depletion of the primer away from the scribe edge was determined using a "traverse depth profile" as described previously [30]. This gives a better indication of where partial depletion occurs because there is an indication of element intensity versus distance from the scribe edge. Traverse depth profiles for 0, 168 and 500 h NSS exposure are shown in Fig. 11(a)–(c), with the traverses themselves superimposed (green rectangles) onto the Li_{479} and Mg_{1369} maps. The depth profiles are constructed by determining the average intensity for each element along lines running parallel to the scribe edge and spanning the primer, such as the blue line in Fig. 11(a). The lines are progressively moved in micron steps from the scribe edge into the primer. The Li and Ba profiles appear "noisy" because larger examples of these particle types are a significant fraction of the length of each line-scan in the traverse and their high intensity contribution leads to bigger values along the line-scan than elsewhere, leading to significant fluctuations in the average intensity along the line-scan and hence the depth profile intensity. Even given the fluctuations the traverse approach provides

better average results for examining depletion than just visual assessment.

The traverses in Fig. 11 (and those for other times) show that the Ti and Ba profiles generally coincide with the scribe edge. On the other hand, the Li and Mg profiles show depletion near the scribe edge. Beginning with the sample without NSS exposure, there appears to be a region around 4 μm in depth that has depleted Li and Mg levels. This is larger than that observed from the SEM (≈ 2 μm) and is likely due to sampling volume effects. In the case of 168 and 500 h NSS, the depletion is evident with both Li and Mg showing decreasing concentrations as the profile nears the scribe edge. In the case of 168 h NSS exposure, the Li concentration is virtually zero at the scribe edge and is considerably reduced within the primer compared to the bulk concentration suggesting both complete (at the scribe) and partial depletion (near the scribe) respectively. The depletion depth for Li is plotted in Fig. 7 along with the other measurements of depletion. This depth is determined by measuring the difference in depth between the Ti and Li profiles at half their height, as shown for Li in Fig. 11 (b) by the black dashed lines. Fig. 7 represents a combination of both complete and partial depletion. It can be seen that for 48 h and longer that the depletion depth is between 10 and 20 μm for all samples. The Mg profiles also indicate similar depletion depths or slightly lower than those determined for Li. Mg depletion has previously been reported for primers containing MgO [60]. The red and black symbols represent two different sets of PIGE/-PIXE data and give an indication of the spread.

In summary the depletion depths estimated from the SEM/EDS results are of a similar order of magnitude to those estimated from the PIGE/PIXE results. However, the methodology for collecting this data focuses strongly on measuring depths using visual assessment of depleted regions. Moreover, the depletion depths have a strong correlation with the mechanical damage caused by scribing suggesting that this is a key factor in the initial release. With the SEM/EDS and PIGE/PIXE results, there is less focus on partial depletion that may occur well away from the scribe edge which is associated with the establishment of a channel network within the primer. The next section focuses on this in more detail.

3.2.3. Partial depletion and network formation

In this section, IBSC sectioning was used to examine changes to the coating as a result of water ingress. Prior to the comparison of observations from the different exposure times an overview of the different types of damage due to water ingress will be given. Fig. 12(a) shows the IBSC section of a coating that has not had any NSS exposure. Examples of the several different types of the inorganic additives are highlighted. For the sample that had no NSS exposure, there was only one pore observed in a Li_2CO_3 particle in over a 300 μm length of primer cross section; essentially there was no evidence of any dissolution of particles,
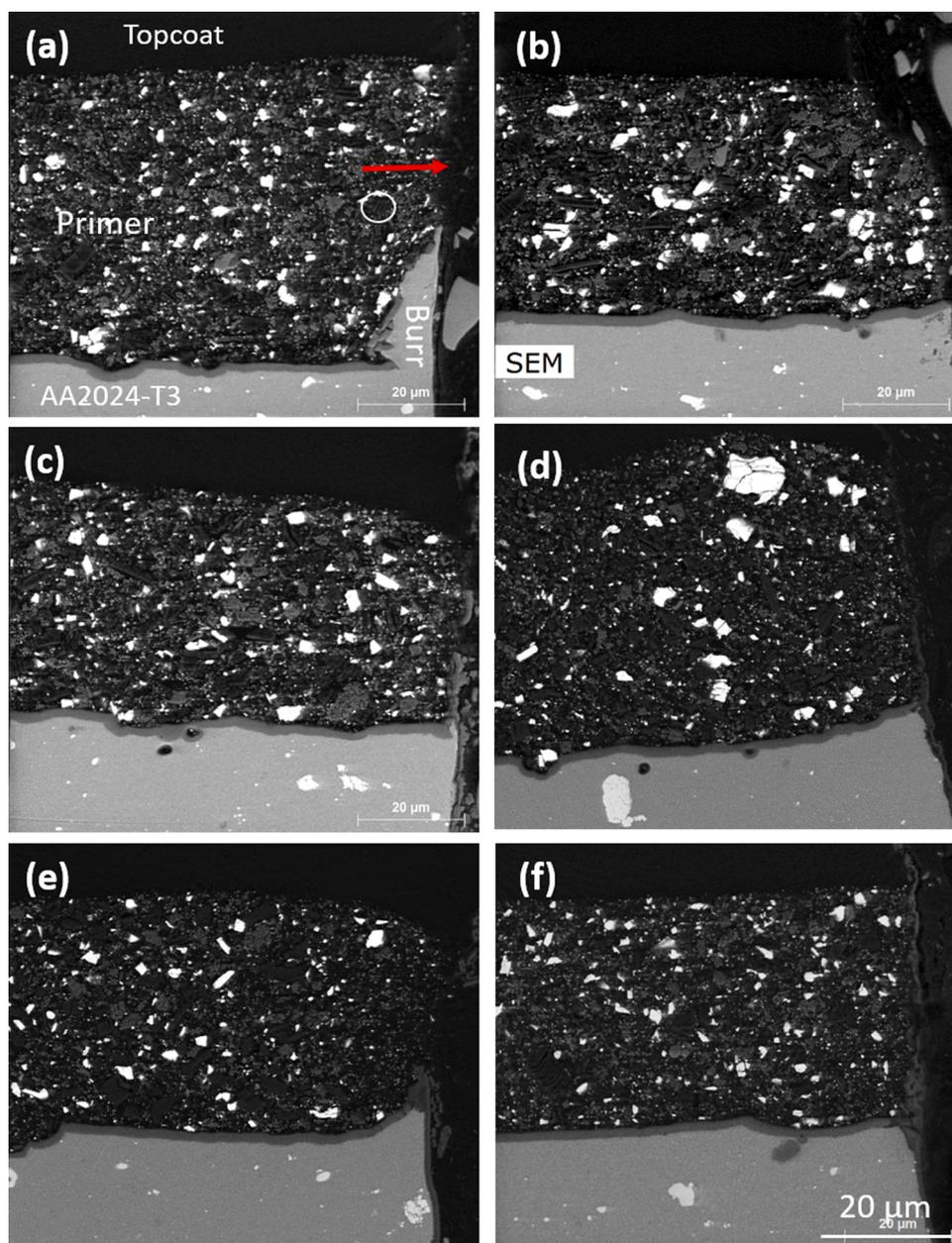
Fig. 5. SEM observations of leached primer as a function of time. (a) 0 h, (b) 8 h, (c) 48 h, (d) 96 h, (e) 168 h and (f) 500 h exposure to NSS. The red arrow in (a) indicates the direction of leaching. The white circle in (a) indicates a dark particle which is shown to be a Li_2CO_3 particle in analyses below (For interpretation of the references to colour in this figure legend, the reader is referred to the web version of this article).

detachment around particles or cracks in the binder beyond the region of mechanical damage at the scribe as seen in Fig. 2. On the other hand, for samples exposed to NSS, there was significant evidence of partial dissolution as described below. Prior to describing the level of dissolution, it is necessary to first cover the changes in the coating as a result of water ingress. Four different forms of attack were observed including:

(i) Local dissolution on the perimeter (red arrows) and interior (red ellipses) of Li_2CO_3 particles
(ii) Detachment (pink arrows) along the boundary between the of Li_2CO_3 particles and the binder, (network forming)
(iii) Cracking (green arrows) in the binder between particles (network forming)
(iv) Some dissolution at the perimeter of $BaSO_4$ particles

Clearly the detachment along edges of particles and cracks in the PU

can be considered as channel network forming events which facilitate the transport of the inhibitor within the primer. Another feature which has not been listed above is that highlighted by the green ellipses. These features were widespread, but not common. They sometimes appeared circular and extended along the Li_2CO_3 boundaries with the PU making them diffuse in appearance. One possibility is that they are electrolyte retained within the coating which subsequently dehydrate under vacuum, however, this is difficult to confirm because of the difficulty of determining whether they contain Li or not. The degree and mix of these different forms of attack depended on the exposure time as well as the distance from the scribe as discussed below.

Fig. 13(a)–(d) display the degree of attack evident on IBSC sections both at different distances from the scribe edge as well as different times. The IBSC sectioning process is assumed to eliminate any possibility of the type of mechanical damage caused by polishing and potentially dissolution effects caused by the polishing medium. This assumption is
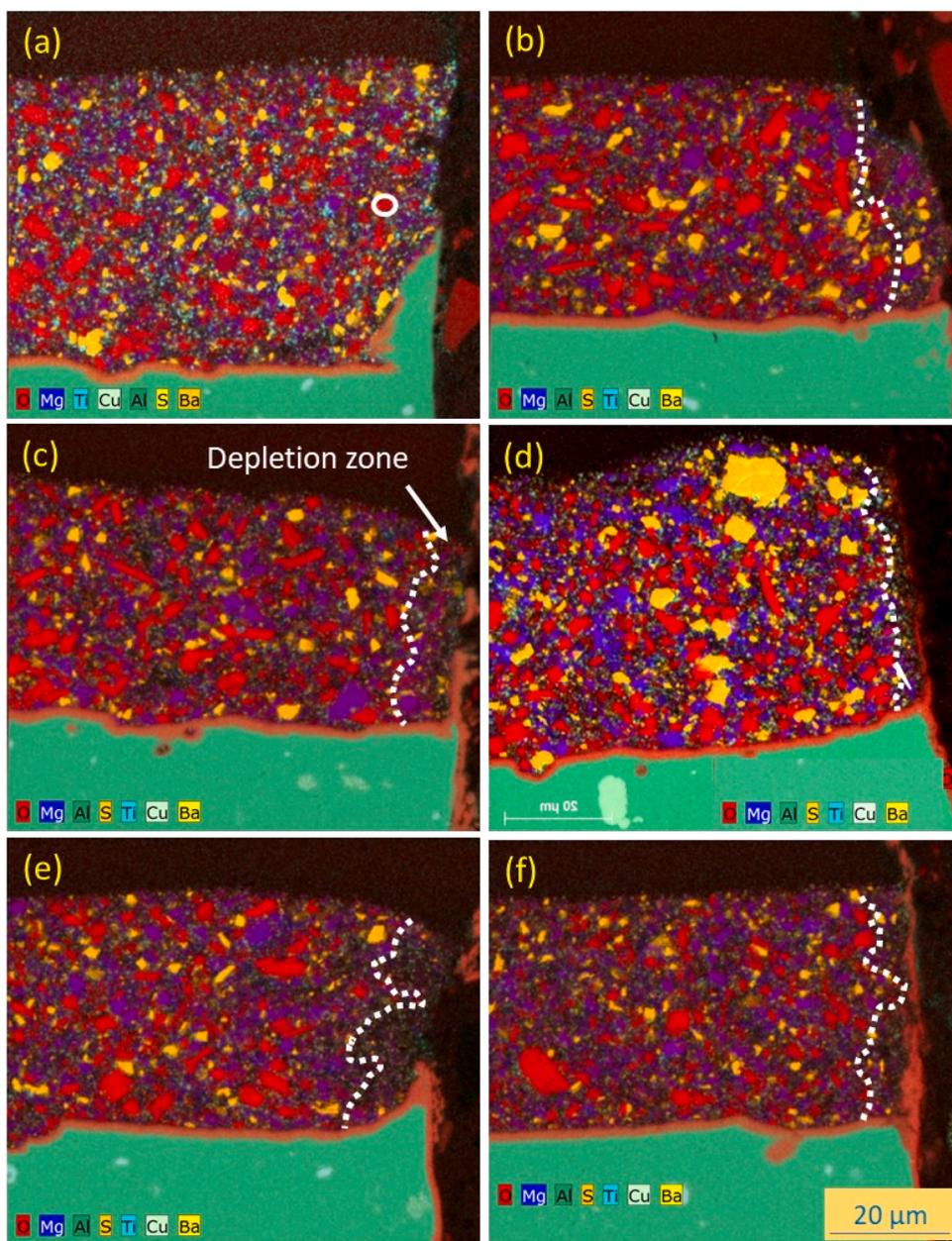
Fig. 6. EDS Quant maps of leaching. (a) 0 h, (b) 8 h, (c) 48 h, (d) 96 h, (e) 168 h and (f) 500 h exposure to NSS. The white circle in (a) encloses an example of a red particle which is shown later to contain Li (from PIGE) and is therefore assumed to be Li_2CO_3 indicating that all red particles are Li_2CO_3. Colour coding for individual elements are included in the maps; the same code is used for all maps. Typical depletion zones are indicated by the dashed white lines in (b) to (f) (For interpretation of the references to colour in this figure legend, the reader is referred to the web version of this article).

largely confirmed, since, as mentioned above, only one pore was found in one Li_2CO_3 particle (Fig. 13(a)) in the sample that had not experienced NSS exposure. This was assumed to be a defect from coating preparation or a pre-existing pore in the particle. By contrast, for the sample that had been exposed for 48 h there were over 200 localised dissolution sites at the PU/Li_2CO_3 interface seen between 100–260 μm and a similar number between 2000–2160 μm from the scribe as indicated by the number of red arrows Fig. 13(b) and (c) respectively, as well as small number of detachment sites (< 20) along the perimeter of these particles (pink arrows in the same figures). The number density for these sites are provided in Fig. 13(e) and (f). Beginning with the 48 h sample, two different distances from the scribe were examined to assess the influence of water ingress. Unexpectedly, partial dissolution of Li_2CO_3 particles was observed at both 100–260 and 2000–2160 μm away from the scribe. Fig. 13(e) shows that the number of sites of partial dissolution (and number density Fig. 13(f)) were similar in both sections. The number of detachment sites was less than 10 % that of the dissolution sites and was the same for both regions. There was no obvious attack on either the TiO_2 or the MgO particles but more will be said on this in the

discussion. There were a small number of sites of localised dissolution around the $BaSO_4$ particles with 10 and 8 sites for the 100–260 and 2000–2160 μm sections respectively. There was also no cracking in the PU in any of these 48 h sections.

After 168 h there were many more dissolution and detachment sites around and in Li_2CO_3 particles than 48 h as indicated by the increase in density of arrows in Fig. 13(d). The respective numbers can be compared in Fig. 13 (e), where it can be seen that there are nearly 120 more attack sites for the 168 h sample compared to 48 h. (Note that these numbers are for attacked particles and not the total number of dissolution sites since some particles have more than one dissolution site). While there is a considerable increase in the number of dissolution sites, there is a much larger relative increase in the degree of detachment around particles indicating that severe attack had penetrated deeper into the primer after 168 h. Moreover, Li_2CO_3-PU detachment was relatively uncommon in the 48 h samples in the ranges of 100–260 μm and 2000–2160 μm away from the scribe edge, but they were 5–6 times more prevalent after 168 h exposure. This supports a view that between 48 h–168 h, networks become more extensive and develop deeper into the
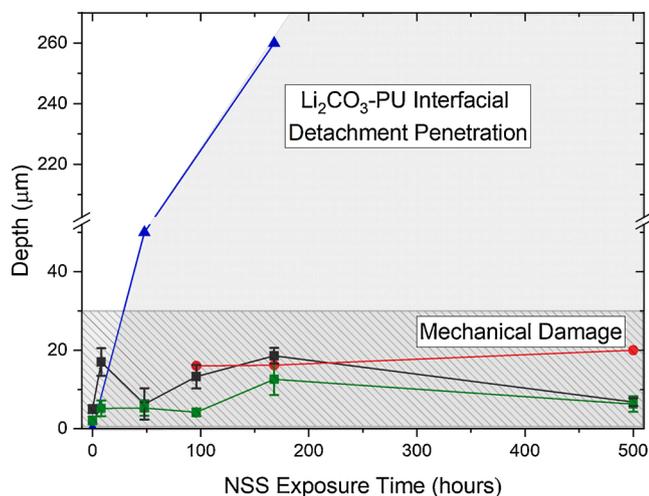
Fig. 7. Characteristic depletion/damage depths for different exposure times to NSS. ■ Depletion depth determined from SEM results, ● leaching penetration determined using first PIGE dataset, ■ leaching penetration determined using second PIGE dataset and ▲ deepest attack (PU-Li$_2$CO$_3$ detachment observation) from SEM ion beam sections. As can be seen in Fig. 6, the depth to which depletion occurs varies considerably. Error estimates of the depletion depth above reflect this variation in depth. The 30 µm depth of the damage region is based on Fig. 2 where damage in the top part of the primer is in the vicinity of 20 µm, but towards the interface with the AA2024-T3 reaches towards 40 µm. Note: error bars only reflect the error in measurement for these sections, other sections with different initial distributions of particles and different levels of damage will have their own characteristic depletion depths.

primer. Cracks in the PU were also observed around 50 µm from the scribe in the 168 h sample but weren't observed in the mechanical damaged region or deeper into the coating. Some cracks are highlighted by green arrows in Fig. 12(c). These PU cracks extend from Li$_2$CO$_3$

detachment or dissolution sites.

As mentioned above there was some evidence of attack at BaSO$_4$ sites. The number of attacked sites increased tenfold in going from 48 h to the 168 h sample. This suggests that BaSO$_4$ sites were becoming active in the development of the channel network development. The surface of BaSO$_4$ particles has previously been reported to be an active site for chromate adsorption in epoxy-based systems [38]. BaSO$_4$ is generally considered to be insoluble or at least sparingly soluble [61] and its role in transport network formation is interesting. In the study of Kopec et al. [38] it was proposed that chromate ions exchanged for sulphate ions since the former was a less soluble compound. In this case the insolubility of the reaction product on the BaSO$_4$ particles doesn't seem to be relevant. Apart from SO$_4^{2-}$ ions, the only other active anions are hydroxyl and carbonate ions. BaCO$_3$ is more soluble and Ba(OH)$_2$ is very soluble compared to the sulphate [61]. This suggests that the relevant surface reaction on the BaSO$_4$ particles in this study is one that leads to anion substitution (CO$_3^{2-}$ or OH$^-$) with the sulphate anion and since both of these species are more soluble than BaSO$_4$ this substitution will lead to reaction and dissolution on the surface of the BaSO$_4$ particles. Of course, the dissolution also leads to void formation which can contribute to channel network formation.

The presence of dissolution in Li$_2$CO$_3$ particles up to 2160 µm into the primer from the scribe would require a diffusion coefficient around 2.3×10^{-7} cm^{2}s^{-1} which is high for water diffusion in PU [62,63]. Thus, the presence of dissolution at this distance from the scribe suggests that transport through the topcoat must also be considered. Using the equation:

$$x = \sqrt{D.t}$$

where x (cm) is the depth into the primer, D is the diffusion coefficient (cm^{2}s^{-1}) and t is the time (s), then the penetration depth from the scribe, using a typical water diffusion coefficient of 1.56×10^{-8} cm^{2}s^{-1} [64] for water diffusion in PU, will be closer to 250 µm and 500 µm for 8 h and 48 h respectively. On the other hand, using the same diffusion coefficient it
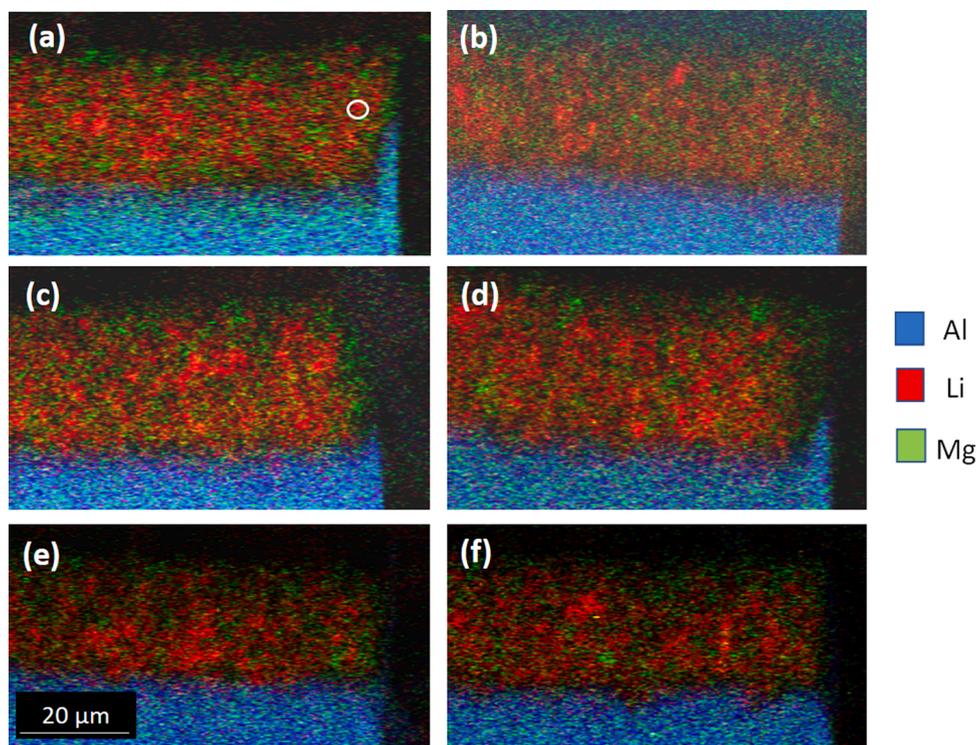
Fig. 8. 3 colour PIGE maps including Li$_{479}$ (red) – Mg$_{1369}$ (green) and Al$_{1014}$ (blue) maps. The granulation in the AA2024-T3 is due to S-phase particles. (a) 0 hours, (b) 8 h, (c) 48 h, (d) 96 h, (e) 168 h and (f) 500 h exposure to NSS. The green particles in the metal are S-phase (Al$_2$CuMg) (For interpretation of the references to colour in this figure legend, the reader is referred to the web version of this article).
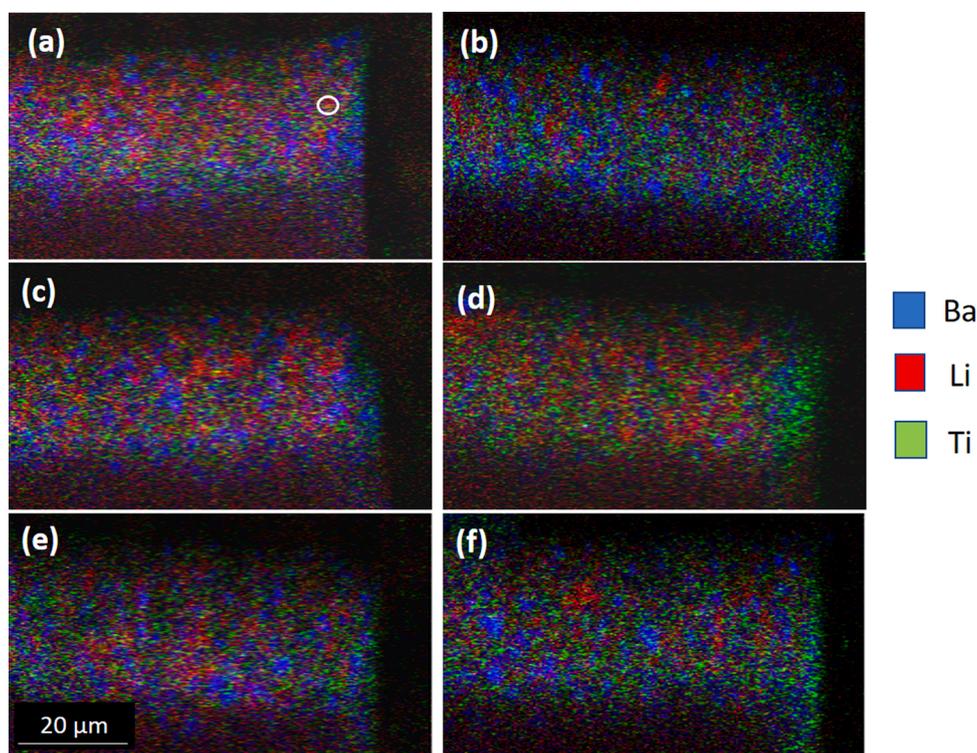
Fig. 9. PIXE-PIGE 3 colour maps. Li (PIGE- 479 keV) red, Ba (L-series X-ray line) blue and Ti (Kα, X-ray) green. (a) 0 h, (b) 8 h, (c) 48 h, (d) 96 h, (e) 168 h and (f) 500 h exposure to NSS (For interpretation of the references to colour in this figure legend, the reader is referred to the web version of this article).
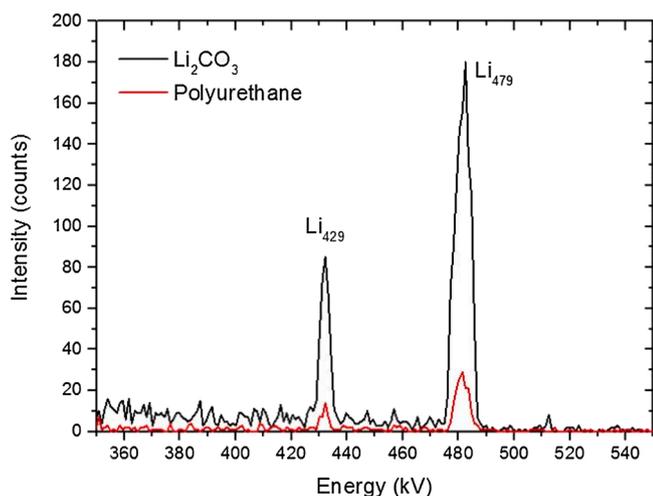
Fig. 10. PIGE spectra from Li_2CO_3 particle (black) highlighted by the white circles in Figs. 5, 6, 8 and 9 and adjacent polyurethane matrix (red) (For interpretation of the references to colour in this figure legend, the reader is referred to the web version of this article).

would only take 5 min for water to penetrate through the 22 μm of the topcoat. Even if the diffusion coefficient was an order of magnitude slower, then it would still only take an hour for water to penetrate the topcoat. Thus, the form of the attack between 2000 and 2160 μm is probably representative of that resulting from water penetration through the topcoat. Since the characteristics of the region 100–260 μm from the scribe are similar (Fig. 13(e)) this strongly suggests that the local dissolution in Li_2CO_3 particles in this region is due to water penetration through the topcoat rather than from the scribe although the latter cannot be eliminated.

From the perspective of channel network formation this leaves only

the Li-PUD sites as the only sites that change significantly in density towards the scribe edge. For example, Fig. 13(f) shows the density ($\#/mm^2$) of different forms of attack at different times and distances from the scribe. It shows that the number density of attacked particles experiencing local dissolution does not change much at the different sites. However, the number density of detachment sites increases markedly towards the scribe. It would seem therefore that these sites are the channel network forming sites.

Thus, the emerging picture is that a zone of very high depletion develops near the scribe interface, probably caused by mechanical damage from scribing, followed by a network of channels that develops deeper into the primer away from the scribe interface via the detachment sites at the Li_2CO_3 particles which also incorporates the local dissolution sites. The maximum depth of attack, defined as the maximum depth where detachment develops at the interfaces between individual particles and the binder, is at least 8 times the depth of complete depletion. Initially the channels appear to develop at sites mainly associated with all Li_2CO_3 particles but begin to incorporate $BaSO_4$ sites as exposure time increases.

3.3. Development of transport network

The data presented up to this point shows examples of complete depletion of Li_2CO_3 particles at the scribe and partial dissolution penetrating away from the scribe (Fig. 11) as well as detachment sites occurring in greater number nearer the scribe (Fig. 13). However, the fact that Li_2CO_3-PU detachment generally occurs at only one face of the Li_2CO_3 particles suggests that there may be a mechanical contribution to detachment and thus to channel network formation. In this section FEA is used to explore the influence of internal stresses within the coating.

The model being considered here is based on rapid water uptake in the coating causing osmotic and swelling pressures. Specifically, at early exposure times it is assumed that water penetration occurs by diffusion through the free volume of the PU from the scribe as well as from through the topcoat causing local dissolution [65]. The assumption that
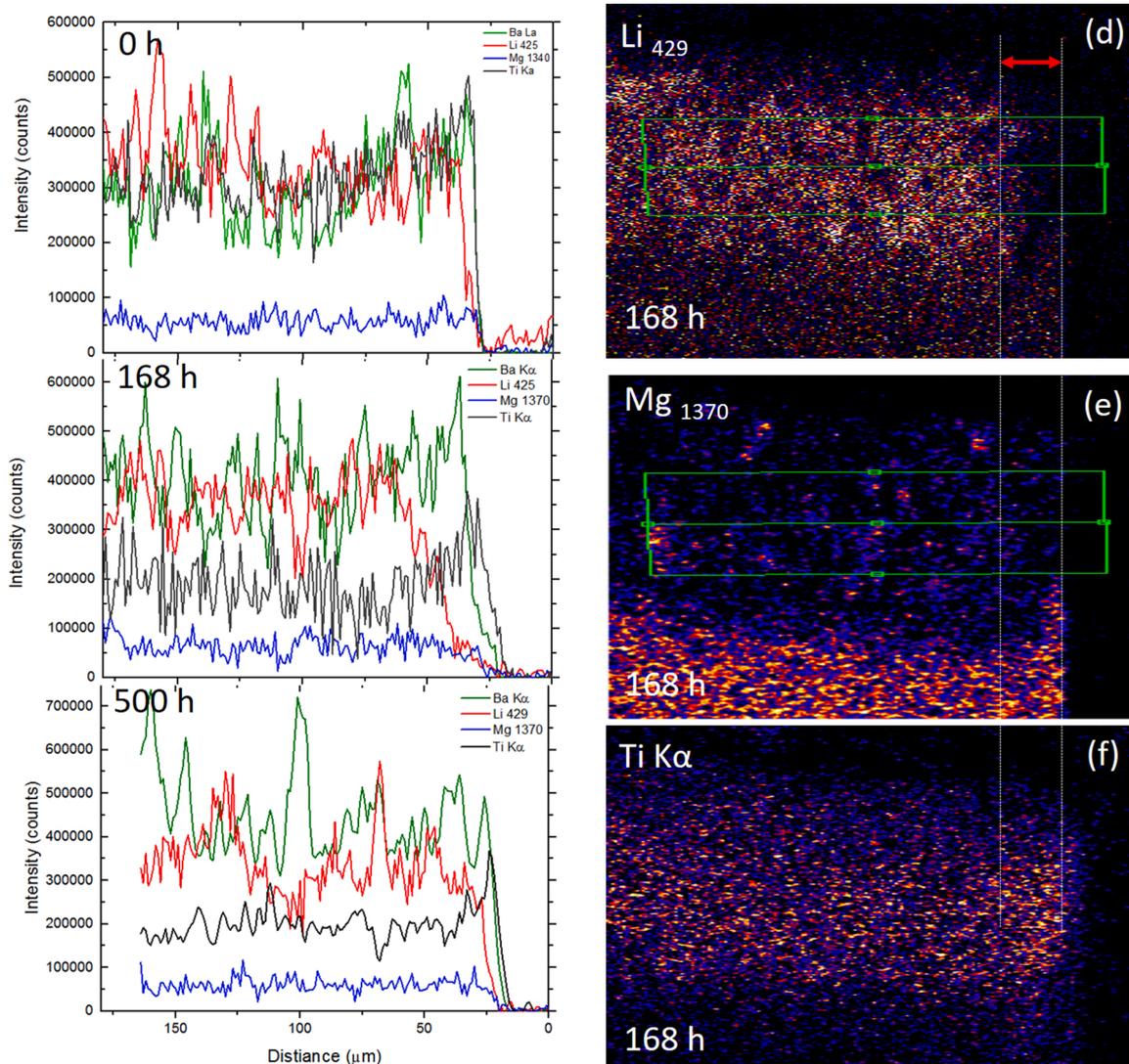
Fig. 11. Example of Traverse depth profile demonstrating the depletion depth plus depth profiles determined using this approach for (a) 0 h, (b) 196 h and (c) 500 h. (d) and (e) show examples of traverses for various maps after 196 h NSS exposure for Li and Mg respectively. The traverse outline is shown in green. The elemental intensity is averaged along the blue line to produce a single value which is the intensity plotted in (a) to (c). The blue lines is then stepped micron by micron along the green traverse rectangle. The red double arrow shows the different between the Ti edge and the Li "egde" which represents the depletion depth. In (a), (b) and (c) the colour coding for the profiles is green: BaKα, red: Li_{429}, blue: Mg_{1370} and black: Ti Kα (For interpretation of the references to colour in this figure legend, the reader is referred to the web version of this article).

it is only water that diffuses through the PU (and not Na^+ or Cl^-) is based on the size of the water molecule (≈ 3 Å) which is smaller than the reported free volume size for PU (≈ 3.7 Å) [66] but that the Na^+ or Cl^- ions are larger than the free volume [30,67]. The data shown in Fig. 13(b) is consistent with this hypothesis, where, after 48 h there is local dissolution at sites in Li_2CO_3 particles but no evidence of a channel network. The presence of water in the PU adjacent to Li_2CO_3 particles leads to local dissolution, meaning that an osmotic pressure may develop at the matrix/particle interface as it dissolves [35]. This concept is based on studies of membranes where membrane swelling is reduced in the presence of a concentrated electrolyte due to the differences in activities of water in the membrane compared to the concentrated electrolyte [31]. (It should be noted that the diffusion coefficient of water may vary with activity as well [62]). For the membrane case, as the external electrolyte concentration increases the driving force for water to enter the polymer is reduced, thus reducing swelling in the polymer. In the situation described here the concentrated electrolyte resides at the particle/PU interface where dissolution has occurred. The "swollen membrane" is the matrix. Water diffuses from the matrix into the

electrolyte which lies in the void, diluting it. Moreover, it is also conceivable that hydration/dissolution reactions of the inhibitor particle may result in swelling that produces a pressure opposite to the osmotic pressure. The pressure difference between the osmotic and swelling pressures (ΔP) (the swelling here related to the inhibitor not of the polymer matrix) may be responsible for the detachment between inhibitor particles and the matrix. It may also be responsible for rupture of the binder causing further void formation. The development of internal stresses upon water uptake in epoxy have also been attributed to the presence with TiO_2 filler [68].

To gain some insight into how ΔP might manifest within the coating, FEA was used to model the effect of internal pressures at sites in the primer. The approach adopted here is different to that used previously [30] where strains were determined around a configuration of particles similar to those observed in the cross sections of coatings. In this case three scenarios are modelled including the influence of the topcoat (Fig. 14), magnitude of the internal pressure and the influence of pressure distribution (Fig. 15).

Fig. 14 shows strains resulting from von Mises stress distributions
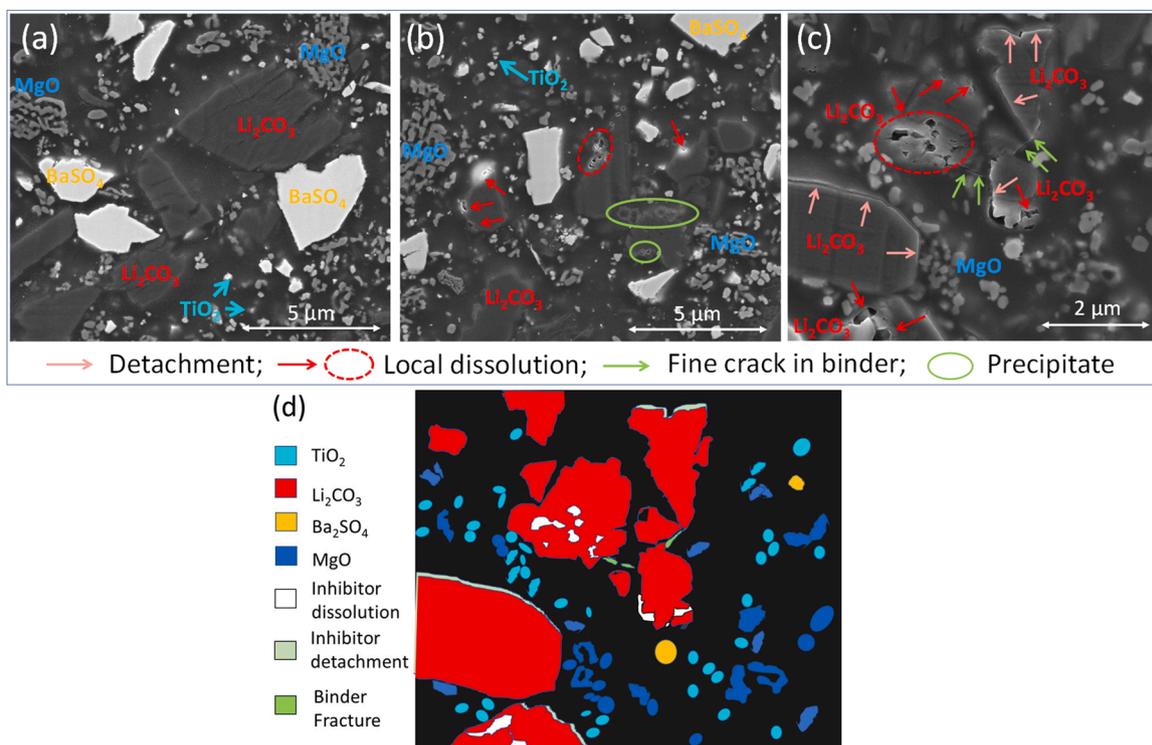
Fig. 12. Secondary electron images of Li$_2$CO$_3$ primer (a) prior to and after (b) 48 h and (c) 168 h NSS exposure around 50 μm from scribe edge. All images have some labelled examples of all types of inorganic particles colour coded as follows: Red- Li$_2$CO$_3$; Orange - BaSO$_4$; Cyan – TiO$_2$ and Dark Blue – MgO. In all images there is only attack associated with either Li$_2$CO$_3$ particles (pink and red arrows and dashed ellipses) or the binder (green arrows and ellipses). (d) schematic of image in (c) highlighting all the forms of damage apart from BaSO$_4$ attack (For interpretation of the references to colour in this figure legend, the reader is referred to the web version of this article).

[56,69] around a configuration of voids and particles without (Fig. 14 (a)–(c)) and with (Fig. 14(d)–(f)) a topcoat. The modelled configurations are shown on the left hand side of Fig. 14 ((a)–(c)) with different colours representing particles with different mechanical properties. The voids are coloured black and labelled. In this analysis the pressure, ΔP, is applied to one face of the void (indicated in red). (Note that these are stains and not displacements in the coatings.) In Fig. 14(b)–(e) the strain goes from highest tensile strain (red) to lowest compressive strain (blue). Comparing Fig. 14(b) and (e) shows that the presence of the topcoat increases the von Mises tensile strain within the primer, concentrating it towards the primer/topcoat interface. On the other hand, the topcoat appears to reduce the shear strain near the primer/topcoat interface but increases it towards the metal/primer interface. It is expected that this increased shear strain towards the metal/primer interface will be transferred to particle/PU interfaces for particles that are near the metal/primer interface. In addition, particles tend to "pin" the strains either along an interface or concentrate it at sharp features (blue circles in Fig. 14 (b) and (e) indicate examples of where strain is "pinned" to an interface). This suggests that the presence of a void with a high enough ΔP may give rise to detachment on an adjacent particle. No doubt detachment would be assisted by weakening of the binder/particle interface due to hydration from water intrusion. This means that Li$_2$CO$_3$ would be the most susceptible particle in this system which might explain why only Li$_2$CO$_3$ particles were observed to have detachment. While there is some indication of strain in the alloy, the magnitude is close to 15 orders of magnitude smaller than that in the coating and hence negligible.

Both the magnitude and direction of ΔP in voids may have a role to play in channel formation. The magnitude of internal pressures within the actual coating is unknown, but work from other studies suggests that they be a few MPa [68,70]. In our previous study only a very small pressure of 0.01 MPa was applied to one face of voids in the FEA

analysis. In this study a range of pressures was examined, of which 0.01 MPa and 10 MPa are presented in Fig. 15(a) and (b) respectively. The particle and void distributions are the same as in Fig. 14. It is clear that over several orders of magnitude the *distribution* of strain within the coating changes little and appears to be localised within the local particle configurations. However, at 10 MPa the *magnitude* of the shear strain is clearly higher with some concentration along the primer/metal boundary. This means that regardless of ΔP the shear strain distribution will depend on the local particle configuration. Clearly a higher ΔP will mean that detachment is more likely due to this mechanical force. While some strain is observed (colour contours) in the underlying AA2024, the magnitude is effectively zero.

In a previous study by the authors and in Fig. 14, ΔP was and is only applied to only one face of the void. In Fig. 15 the influence of pressure applied to all faces of the void is also examined. It can be seen in comparing Fig. 15(c) and (d) that the strain distribution is clearly more intense and extensive around the void when ΔP is applied equally to the four faces of the voids. Interestingly, the regions of high strain are still limited by the local particle configuration again highlighting the importance of particle distributions. The other aspect to note is that the strain at the primer/metal interface also intensifies as it does with particle/PU interfaces. The strain level in the metal below the bottom void (red arrow in Fig. 15(d)) while larger than in Fig. 15(c) is still very small and effectively zero. However, clearly the strain at the interface between the primer and the AA2024 is significantly higher indicating that the boundary also "pins" the strain thus making it more susceptible to detachment. Detachment along this interface was not observed experimentally and the authors attribute this to the anodised layer which is not included in the modelling. On the other hand it is possible that the strain might further increase around the inorganic particles near this interface. There may be some preliminary evidence to support this since the ratio of delamination in the bottom to top halves of the coating for the 168 h
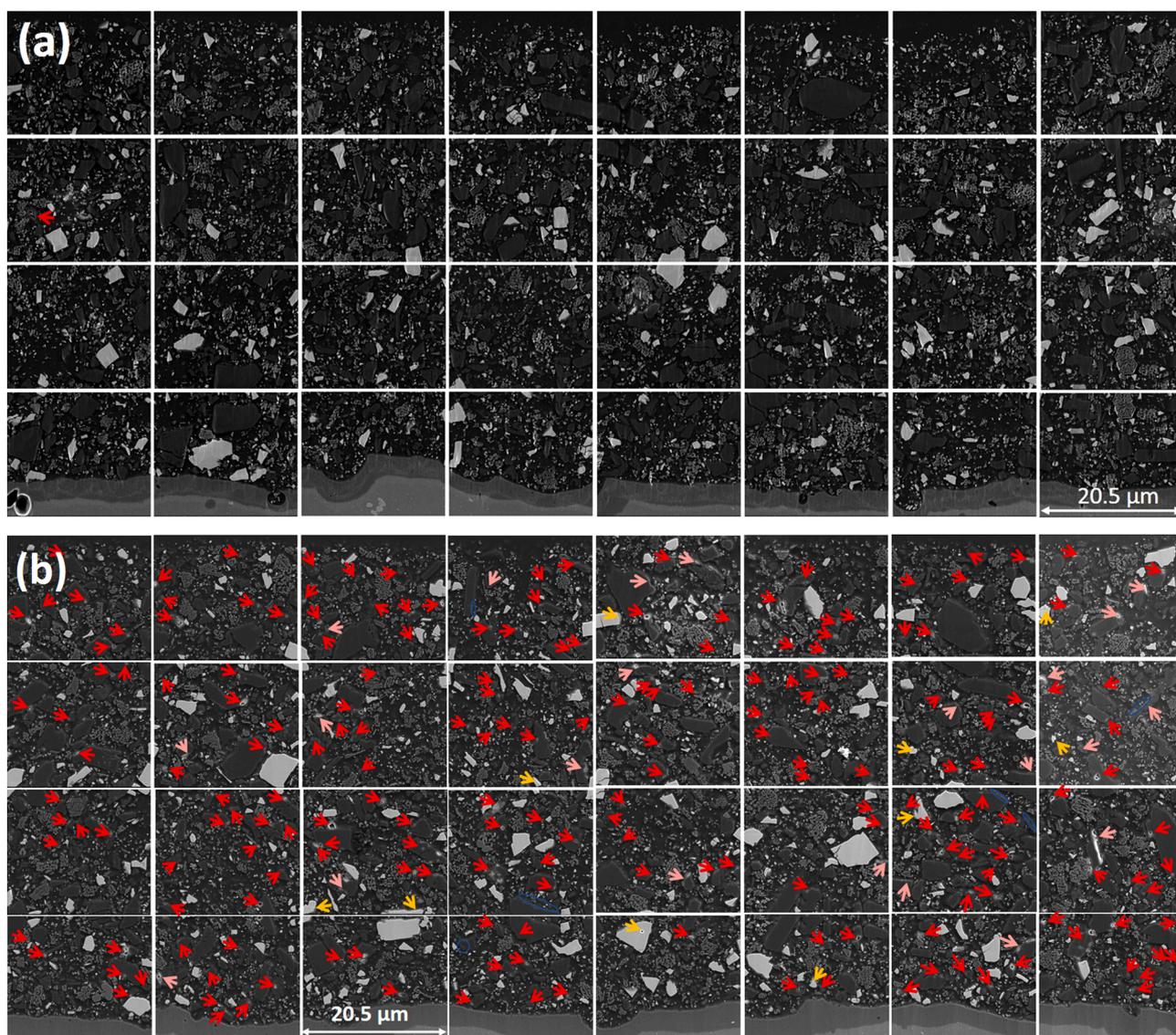
Fig. 13. Montage secondary electron images of IBSC sections of coatings after different exposure times to NSS. (a) no NSS exposure (100–260 μm from the scribe), (b) 48 h (100–260 μm from the scribe), (c) 48 h (2000–2160 μm from the scribe)and (d) 168 h NSS exposure (100–260 μm from the scribe). Red arrows indicate localised attack around Li_2CO_3 particles, Light red arrows indicate detachments around Li_2CO_3 particles and orange arrows are attack at $BaSO_4$ particles. NB there is only one arrow per attacked particle even if there are multiple sites on the particles. (e) indicates total number of sites broken down into local attack (Local) and detachments for three different NSS exposure times and two different distances away from the scribe for 48 h NSS. (f) is a comparison of the site densities of the different forms of attack (For interpretation of the references to colour in this figure legend, the reader is referred to the web version of this article).

(100–260 μm) sample was 1.5, but this should be considered a preliminary result. In summary, the results of all the FEA studies presented here indicate that the primer/metal interface as well as PU/particle interfaces near the primer/metal interface may produce the most susceptible sites to mechanical degradation as a result of ΔP.

3.4. Leaching behaviour of the system

Having looked at the development of transport networks within the primer we turn to the release of various soluble components into the external electrolyte. In this case the leaching experiments are performed during immersion. Li, Mg and Ba were all observed in the leachate solution and their accumulated release profiles are plotted in Fig. 16(a). Lithium had a rapid increase at short times up to 10 h, but then slowed markedly with increased time. Mg release was slower and still increasing after 196 h exposure to distilled water. The Ba release was at a much lower level than either the Li or Mg and was also still increasing at 196 h.

The *instaneous* Mg/Li and Ba/Li molar ratios (based on the difference between the current and previous values) are plotted in Fig. 16 (b). The Mg/Li molar ratio increased at short times to a peak of~ 1.2 in the first 10 h then further increased to~ 2.2 around 25 h but thereafter gradually decreases to a value of~ 1.5 at 196 h. This indicates that, at 196 h there was considerably more Mg accumulating in the leachate than Li. It should be noted that AA2024-T3 contains Mg and it is expected that this will make a contribution to the Mg in the leachate, but there is also some Mg coming from the primer as indicated from the depth profiles. The Ba/ Li ratio showed a similar behavior, but the absolute molar ratios were much smaller because of the lower amount of Ba released.

As reported previously [30,46,71–73], the release can be described by a power law where the mass released is proportional to t^n ($M = kD_{eff}t^n$) where the proportionality constant is proportional to the effective diffusion coefficient (D_{eff}) and n is an index that reflects the kinetic behavior dictated by the porosity of the structure from which ions are released. In our previous work a range of different n values were found
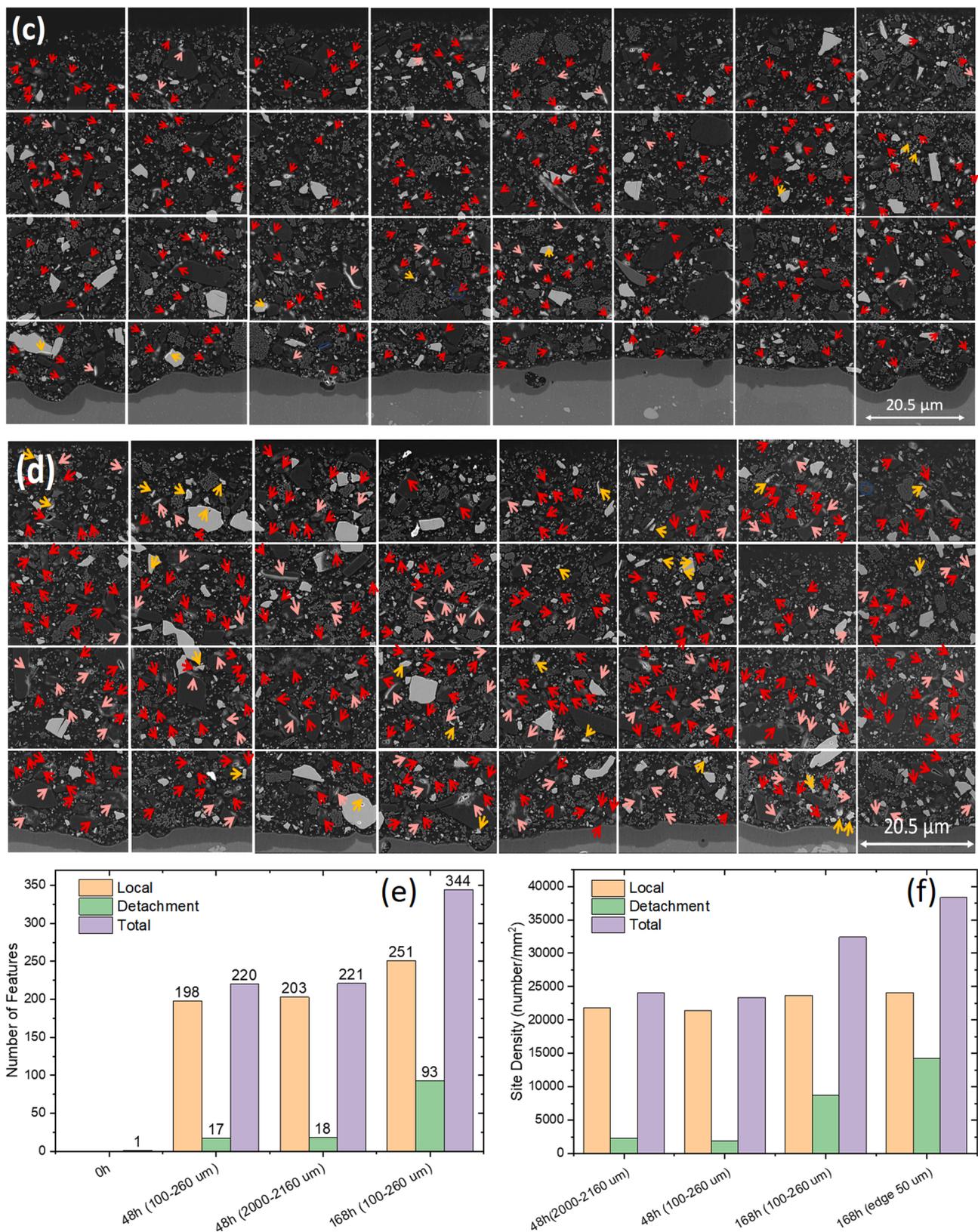
Fig. 13. (*continued*).

for Li, Mg and Ba release from the Li$_2$CO$_3$ primer [30]. Common values for n are: $n < 0.33$ suggested leaching from a void structure that is fractal in nature [74] and has reached its percolation limit, $n = 0.5$ reflects Fickian diffusion and $n > 0.5$ reflects a significant amount of direct dissolution into the electrolyte from the primer. The release will also be subject to other phenomena which can influence the level of inhibitor release into the leachate. These include reactions in the scribe which will consume leached components of the primer as well as transport barriers at the cut face of the scribe such as those described in Fig. 3 and Mg release from the scribe due to corrosion.
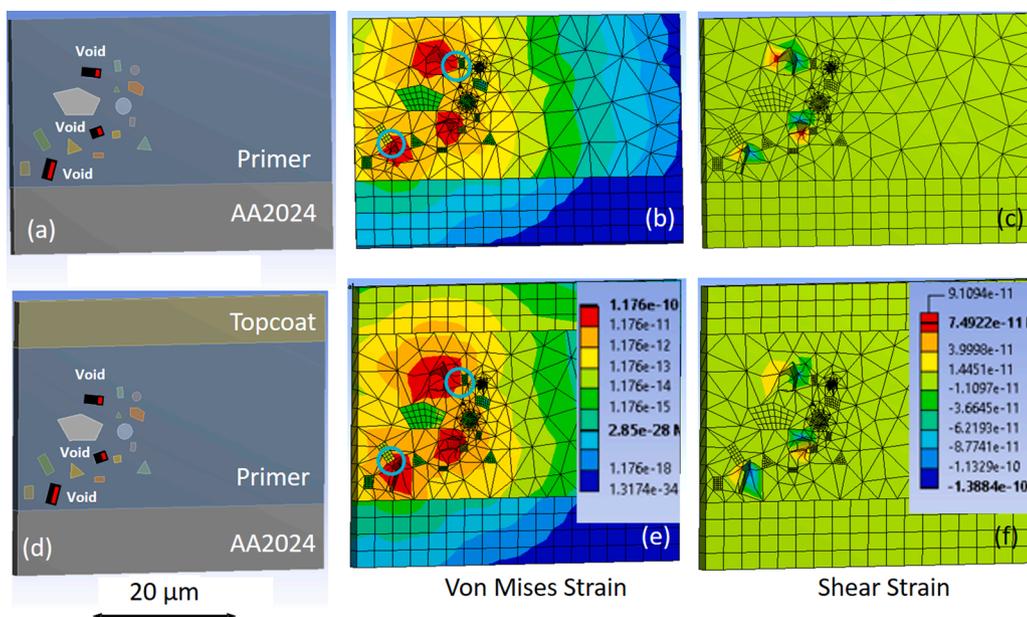
Fig. 14. FEA analysis of von Mises and shear strain distributions in the primer without and with a topcoat. Note that the strains are very small – these are not displacements. (a) configuration of particles and voids for FE analysis, (d) configuration with top coat. The particle and void distributions are the same for both models, but (d) explicitly includes the topcoat. The voids are labelled and coloured in black and red (a) and (d). The red indicates the face to which ΔP is applied. (b) and (e) strain distribution based in von Mises analysis for particle configurations in (a) and (d) respectively. (c) and (f) shear strain in the XY plane for particle distributions in (a) and (b) respectively. Scales are in mm/mm with the von Mises strain scale going from tension (red) to compression (blue) (For interpretation of the references to colour in this figure legend, the reader is referred to the web version of this article).
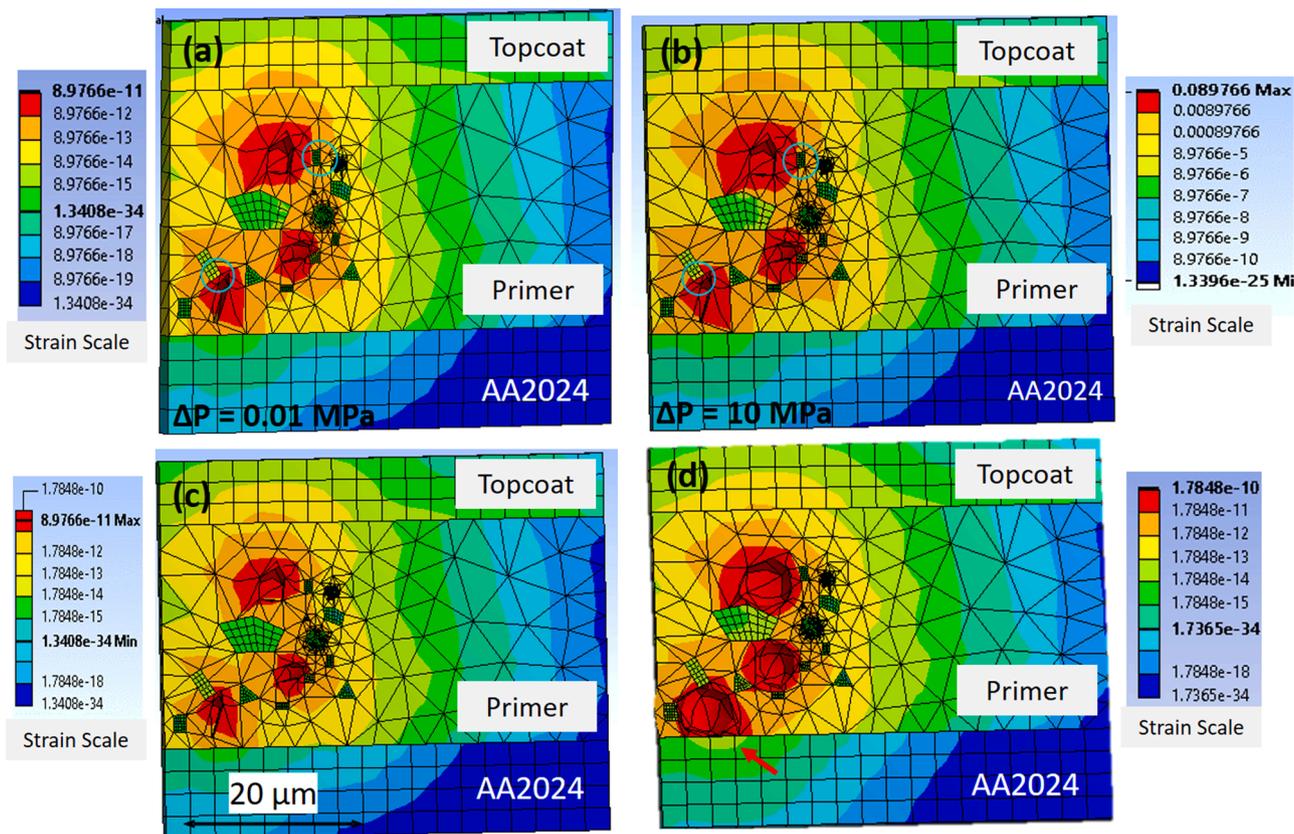
Fig. 15. FEA analysis of von Mises strain distributions for a primer/topcoat model. Comparing strain distribution under different applied pressures of (a) 0.01 Pa and (b) 10 MPa. Comparing strain distribution when the stress is applied to (c) one face and (d) four faces of the void. Blue circles indicate some examples where strain is "pinned" to a particle interface (For interpretation of the references to colour in this figure legend, the reader is referred to the web version of this article).

The index n can be determined from the gradient of a plot of $Log_{10}(M)$ versus $Log_{10}(t)$ [71]:

$$log_{10}(M) = Log_{10}\left(kD_{eff}\right) + nlog_{10}(t) \qquad (2)$$

The data as represented by Eq. (2) for Li, Mg and Ba are plotted in Fig. 16(c). n is effectively the gradient of this line at any point in time

and is plotted in Fig. 16(d). The data in Fig. 16(c) show that there are different behaviours for Li and Mg at different times. For Li there appears to be two regimes as indicated by the straight red dashed lines (Fig. 16(c)). Initially n is between 0.7 and 0.8 which indicates a mixture of direct dissolution and Fickian diffusion indicating very rapid release kinetics (Fig. 16(d)). This most likely represents release from the
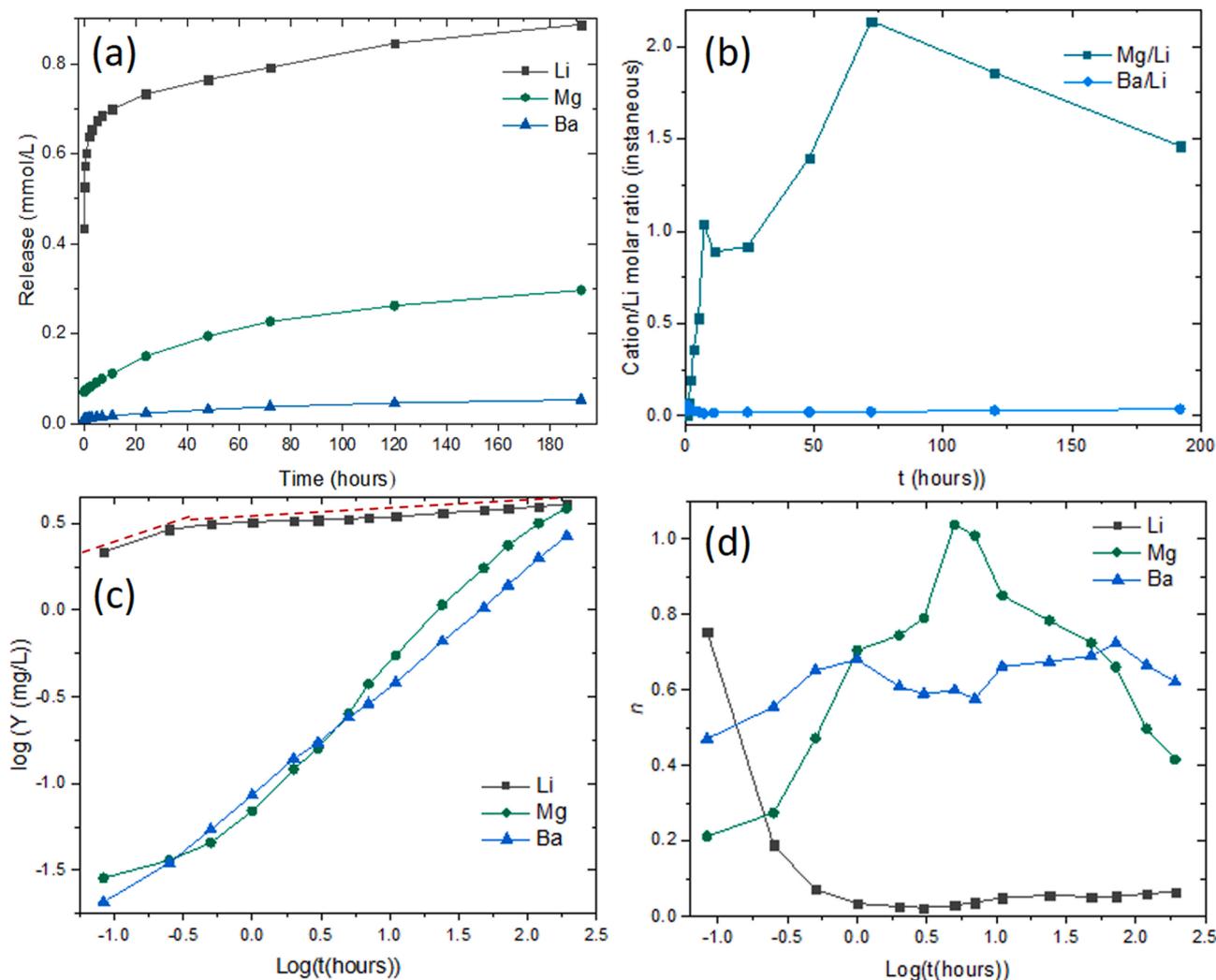
Fig. 16. Leaching data from the cut edge of a scribe through the topcoat/primer. (a) accumulated species in mmol/L, (b) molar ratio of Mg/Li, Ba/Li and total Li accumulation (for reference), (c) leach rate Li, Mg and Ba and (d) value of n for Li, Mg and Ba specified in different time regimes.

damaged edge of the primer where mechanical cracking directly exposes Li_2CO_3 particles to the electrolyte. It should be noted that most of the detachment caused by mechanical damage was at Li_2CO_3/PU interfaces thus "preferentially" exposing these particles to the electrolyte. For times longer than 1 h the value of n for Li is close to zero indicating that very little Li is entering the leachate solution. This could be explained by a number of effects (i) the exhaustion of the leachable Li reservoir, (ii) consumption in the scribe, (iii) no further penetration of a channel network at this time or that (iv) that the oxide covering the cut edge of the primer effectively blocks further release. Clearly from the SEM there is considerable Li_2CO_3 remaining in the coating so it can't be exhausted, but perhaps some insoluble layer has formed on the surface of particles. With respect to (ii) while LDH formation occurs over this same time span there is no evidence that the rate of formation increases rapidly after 1 h nor lasts indefinitely. With respect to the channel network (iii) it clearly continues to develop with increasing time. With regard to (iv) oxide formation over the edge of the primer clearly forms a barrier, so this may well be responsible for the reduction in the rate of Li leaching.

The release of Mg (Fig. 16 (c)) shows a gradually increasing trend different from that of Li. It should be noted that Mg release should be considered in the context that there may be Mg in the leachate as a result of corrosion of the underlying AA2024-T3 in the scribe. At short times the value of n was close to 0.2 indicating that either initially the MgO is not very soluble or perhaps inaccessible from the PU matrix consistent with the SEM observations. No significant detachment around Mg-oxide

particles was caused by mechanical damage indicating that the Mg-Oxide/PU interface is strongly bonded. Low solubility of additives was a factor given that low n values reported by Klomjit and Buchheit [72] for chromate release. At intermediate times n changes to 0.8 to 0.9 indicating much higher release perhaps including some direct dissolution from the primer. This increase occurs at similar times to the drop in Li release, perhaps suggesting a decrease in pH allowing for an increase on the solubility of Mg-containing compounds. This is supported to some extent by the observation using SEM, EDS and PIXE maps that Mg depletion zones develop, but that they appear to be confined to mechanically damaged region. At longer times the Mg release reverts to $n = 0.5$, but attributing this to Fickian diffusion is problematic since films cover both sources of Mg (AA2024 and Mg in the primer). For example, as can be seen in Fig. 17, the edge of the scribe is covered with a duplex layer comprising an inner layer which is probably HT or p-B and an outer layer labelled Al-oxide-hydroxide [7,8]. This outer layer is likely to be a gel during exposure to the electrolyte. Similar layers are formed in the scribe itself meaning that interpretation of the Mg leaching data is not straight forward.

The Ba data appears to be fitted with a single line over the entire timeframe in which data was collected. The value of $n = 0.64$ ($R^2 = 0.99$) suggesting a mixture of Fickian diffusion and direct dissolution into the leachate solution.

As a note on leaching from the scribe, the damage caused by scribing, while accurately reflecting what occurs during mechanical damage to a
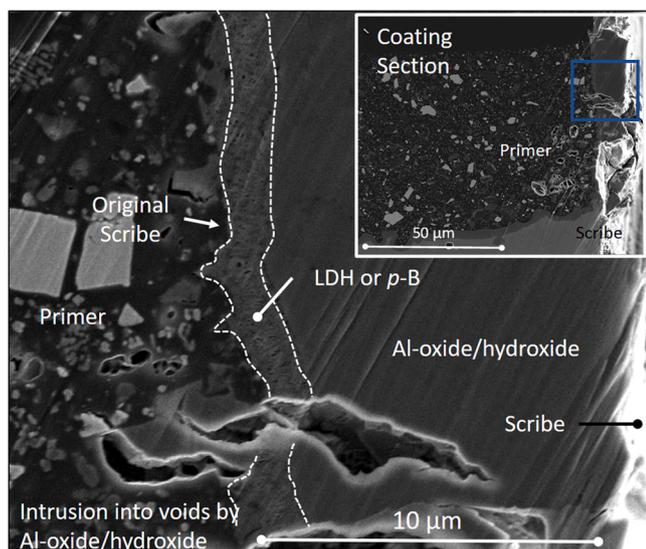
Fig. 17. SEM image of a cross-section of the scribe edge from the sample exposed for 168 h to NSS. The inset shows in blue the region in the main image. At the scribe edge there is a duplex layer covering the primer edge consisting of a porous inner layer (probably LDH or p-B and an outer layer of Al oxide/hydroxide) [7,8]. There are points along the edge of the primer where apparently the Al-oxide/hydroxide appears to have penetrated the primer through the inner layer. There is also cracking in oxide which penetrates into the primer (For interpretation of the references to colour in this figure legend, the reader is referred to the web version of this article).

coating in-service, may not be the best configuration for measuring intrinsic leaching properties. In fact an experimental arrangement such as cut edge corrosion experiments where a polished surface is used would be a better method for collecting data in order to separate leaching from the effects of mechanical damage to the coating edge and the influence of corrosion in the scribe on leachate concentrations [75].

4. Discussion

4.1. Overview

In this paper the authors have investigated the leaching of Li_2CO_3 and other components from a scribe through a topcoat/primer/metal system. The experimental observations are summarised in the model in Fig. 18. The leaching has been interpreted in terms of the development of a network of transport channels based on PIXE, PIGE, EDS and SEM results on IBSC sectioned samples. These channel networks are formed through (i) mechanical damage at the scribe edge, (ii) dissolution associated with clusters of particles and (iii) rupture of the binder due to development of internal stresses. There are two aspects to these internal stresses. First, an osmotic pressure develops across the interface of the binder with the inorganic particles. It is proposed that the osmotic pressure develops because the uptake of H_2O molecules is much faster than ions from the external electrolyte meaning that the binder becomes saturated at an early stage. H_2O is then driven under a chemical potential gradient into the developing electrolyte at the interfaces with inorganic particles. This type of reaction is also apparent well away from the scribe (observed up to 2700 μm from the scribe) where it is attributed to H_2O diffusion through the topcoat which facilitates the dissolution reactions. This type of reaction was described by Sinko nearly 20 years ago [35]. The second aspect is associated with the swelling due to electrolyte at sites around Li_2CO_3 particles, which is opposite to the osmotic pressure. The difference between these two pressures, ΔP, is the driving force and its magnitude will probably change with time. The slower development of partial detachment around some particles is also consistent with an increase in ΔP and internal stress distributions among

clusters of particles as seen in FEA modelling. These dissolution reactions, deep in the primer, are not an artefact of electron beam interaction with the samples (particularly the Li_2CO_3), since no such attack was observed in a sample which had not been exposed to NSS. The water interaction is predominantly with Li_2CO_3 particles and to a much lesser extent with $BaSO_4$ particles. It is noteworthy that the detachment between some interfaces of the Li_2CO_3 particles and the PU increases with time at locations near the scribe and also penetrates further away from the scribe (Fig. 18, bottom). Closer to the scribe fine cracking in the PU itself further contributes to network development. These changes strongly suggest that the Li-PU detachment are the network forming structures, which, as they penetrate deeper into the primer, incorporate the local dissolution sites.

One further comment on ΔP relates to whether it is responsible for the high initial Li release into the scribe. It is feasible, in the early stages of leaching that ΔP might drive expulsion of the Li_2CO_3 dissolution electrolyte from the channel network close to the scribe. This would lead to very high initial n values as observed during the early stage of leaching. As the Li_2CO_3 dissolution product is expelled the driving force diminishes and the leaching process reverts back to diffusion, albeit through a continually modifying channel network.

4.2. Unresolved questions

The presence of only localised dissolution on some Li_2CO_3 particles at the beginning instead of dissolution of all particles needs further comment. It would seem that if the PU is saturated then attack should proceed evenly around the perimeter of the all particles. Alternatively, if the water ingress is via the interfacial boundary between the Li_2CO_3 and the PU then general dissolution along this interface could also be expected. However, what is observed is that there are local dissolution sites within particles and occasionally much more extensive dissolution of particles. This suggests heterogeneity at the Li_2CO_3-PU interface. Some causes of heterogeneity might include the following: First, the Li_2CO_3 particles themselves may be heterogeneous. These particles are crystalline (EBSD patterns were obtained but not shown) and displayed some faceting (electron channelling contrast was observed and an example of which is shown in Fig. 19(c)) but were otherwise homogeneous under SEM examination. Some indication of the internal structure of the particles (perhaps faceting) can be seen in Fig. 19(c) where internal structure is evident in the central Li_2CO_3 particle. However, there was no evidence of a correlation between the local dissolution sites and the faceting so it seems unlikely that the particles themselves have intrinsically susceptible sites. The PU itself may have internal structures which change the local free volume thereby influencing the local water concentration. Variable structures on a range of scales have been reported for PU [63,65,76,77] and epoxies [74,77–81] which influence the water distribution within coatings suggesting that the PU itself may be responsible for a heterogeneous distribution of water at the interface. Certainly, at the submicron scale, as can be seen in an EDS Carbon map of the primer (Fig. 19(a)), the PU can probably be considered as sponge-like in this high solids primer. The wall thickness between some particles is well below 500 nm. Whether such thin layers can be considered as "bulk" PU with water diffusion properties of "bulk" PU or whether it should be considered interfacial with modified properties is unclear but clearly warrants further investigation. Finally, the distribution of additives such as surfactants and wetting agents may also be very heterogeneous over the particle/PU interface leaving some sites more susceptible than others to local dissolution. The data presented here, however, offers no insight into which mechanisms might be responsible for the local dissolution in the Li_2CO_3 particles, but they warrant further investigation. Presumably, once a site is initiated it reduces the probability of a second site initiating nearby (in the short term at least) because of the withdrawal of water from the PU matrix into the developing electrolyte.

Clearly, the interface between the Li_2CO_3 particles and the PU is the
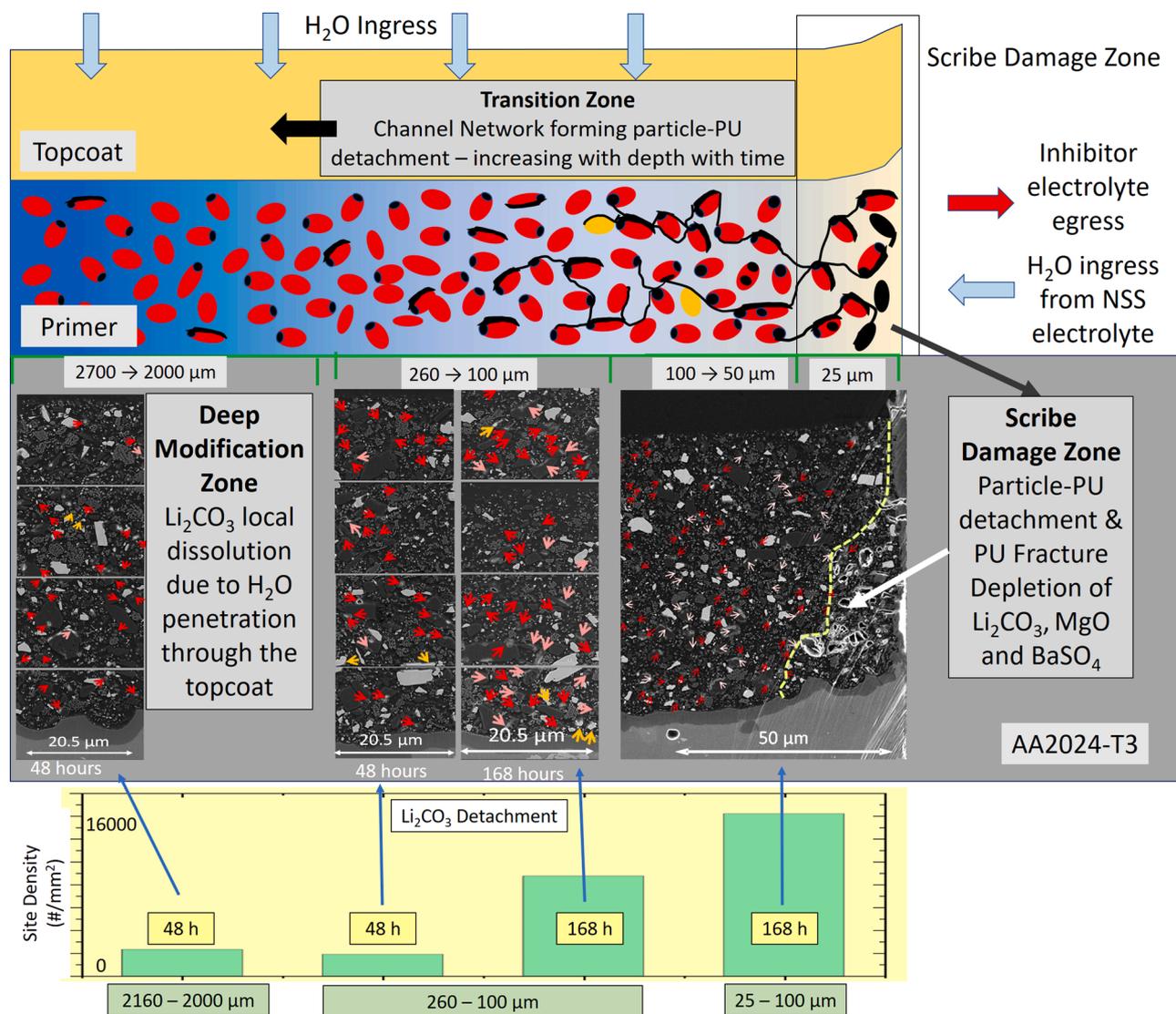
Fig. 18. Schematic representation of leaching characteristics of a top-coated primed AA204-T3 substrate. Top is a schematic of the topcoat (orange) covering the primer where red particles represent Li_2CO_3, yellow are $BaSO_4$ and black marks indicate void and channels. The TiO_2 and MgO particles have not been included for clarity. The AA2024-T3 is in grey beneath the primer. Superimposed on the AA2024-T3 are SEM images from Fig. 13 indicating the type of damage observed (coloured arrows) at the representative depth. At the bottom is a graph showing the level of detachment at different times and locations away from the scribe (For interpretation of the references to colour in this figure legend, the reader is referred to the web version of this article).

target interface for the development of a channel network for the transport of the inhibitor. The mechanical bond at the particle/PU interface is apparently weaker than other interfaces in the primer since this is the one where detachment occurs, although in most cases it is only along a single face which is consistent with detachment due to stress concentration around particle clusters as seen in the FEA. The detachment only at the Li_2CO_3-PU interface also confines channel network formation to Li_2CO_3 particles thus creating inhibitor clusters.

The level of Mg release is also an area that is clearly complicated. First Mg ions are detected in the leachate and a Mg depletion zone is detected to various depths using PIGE and EDS. On the other hand SEM examination shows little attack around MgO particles in the coating, even 20 microns or so from the scribe interface. So there is a question about what is happening to Mg^{2+} ions in the coating at the scribe. While Mg^{2+} release has been reported for MgO containing primers [48] that was a simpler system than that described here. The high solubility of Li_2CO_3 means that the electrolyte that develops at the Li_2CO_3-PU interface will be close to saturation with Li^+ and CO_3^{2-} ions. If MgO particles are dissolving in addition to $BaSO_4$ particles, then the electrolyte at this interface could be quite complex. Mixed electrolytes close

to saturation may have complex precipitation cycles at these interfaces resulting in precipitate accumulation other than Li_2CO_3. Studies on precipitation of Li_2CO_3 from brines containing Li^+, CO_3^{2-}, Mg^{2+}, O^{2-}, and SO_4^{2-} ions show that other cations and anions can have a significant bearing on Li_2CO_3 precipitation [82]. The complex solution interfacial chemistry may mean that Mg compounds may well precipitate at Li_2CO_3 interfaces and surface phases may develop on the MgO particles (e.g. $MgSO_4$ replacing MgO or $Mg(OH)_2$). These type of surface phases have been observed before with surface sulphate phases on $SrCrO_4$ particles reported as a result of the development of interfacial electrolytes [38]. This complex area is therefore the subject of further investigation.

Another unresolved issue from this study is that dissolution product seems to be absent in many of the local dissolution sites in the Li_2CO_3 particles, although there are some sites where dissolution product is observed such as the sites in the Li_2CO_3 particles indicated by the blue arrows in Fig. 19(c) and (d). One possibility is that these sites were filled with liquid electrolyte which has dissipated during the IBSC sectioning. However, it might be expected that the evaporation of a liquid electrolyte would leave a (inorganic) residue. What is more likely is redistribution to other sites within the channel network. If these sites are
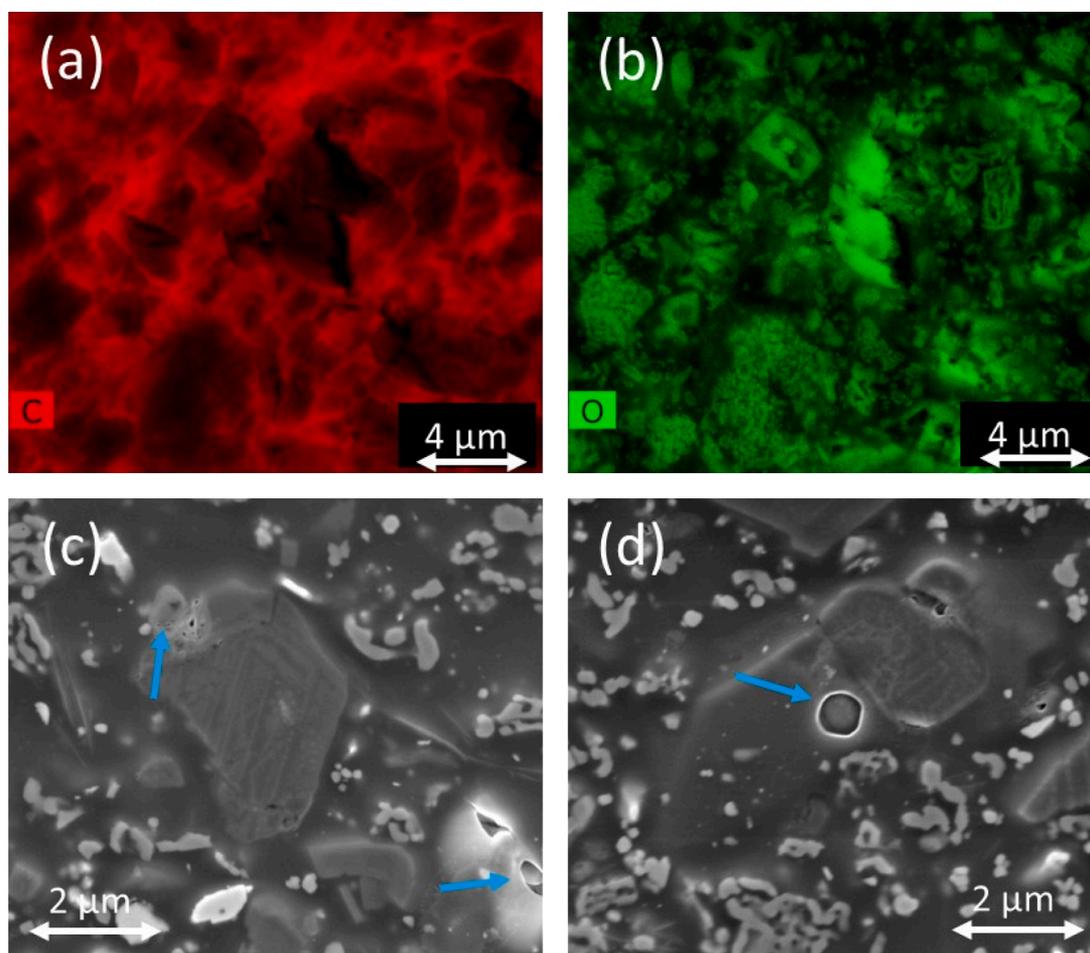
Fig. 19. (a) C and (b) O EDS maps from the sample with 48 h NSS exposure 2.7 mm away from the scribe. The oxygen map shows the position of inorganic particles whereas the C map highlights the PU matrix. (c) and (d) examples of dissolution product at the perimeter (c) and inside Li$_2$CO$_3$ particles (c) and (d) for the 48 h sample. (c) and (d) are not the same region as (a) and (b).

connected to the scribe via a channel network then it is possible that the electrolyte has been discharged into the scribe. This may well be the case for sites closer to the scribe where the channel network formation through detachment has occurred. On the other hand, for sites that are observed millimetres away from the scribe it seems unlikely that the channel network develops that deep into the primer where little Li$_2$CO$_3$-PU detachment is observed, so the dissolution product is more likely to be redistributed elsewhere in the primer. Redistributed Li-containing dissolution product may not be so easy to observe. One difficulty with this particular primer system is the problem of detecting Li. This means that if Li dissolution product is redistributed in this way then it will not be obvious in the SEM or even in the PIGE measurements. Nevertheless, close examination of some sites around Li$_2$CO$_3$ particles show features that could be related to redistributed dissolution product that have a different morphology to the particles themselves and are also not observed on the sample without NSS exposure. One these types of sites is indicated by the top blue arrow in Fig. 19(c) where it can be seen that there is an irregular shaped features siting on the interfacial boundary between the Li$_2$CO$_3$ particle and the PU. If these types of sites are redistribution sites then it is not clear what the driving force would be for local relocation of the dissolution product. The primer itself swells during water uptake perhaps local differences in the rate of swelling causes local redistribution of dissolution product. Another possibility to explain the missing dissolution product is that Li ions themselves become incorporated locally in the PU as part of the swelling process.

4.3. Geometric considerations when comparing leaching from a scribe interface to that from the primer surface

The leaching model presented above is silent on the geometry of the scribe edge compared to the surface of a primer. Clearly there are geometric differences between the primer exposed at scribe edge versus that exposed on an external surface of the primer without a topcoat. In the absence of mechanical damage, the scribing process will intersect clusters randomly. For the larger clusters this will mean that the remaining part of the cluster may well penetrate up to a few hundred microns away from the scribe edge. This situation is different to the primer-only case where the dominant "characteristic length" is the primer thickness and the cluster may have many more particles "intersecting" the external surface. Transport behaviour through the channel network is likely to be the same. However, the FEA analysis provides some insight into how the net pressure difference ΔP, manifests within the coating. Generally, the topcoat increases the equivalent elastic strain at the *primer/topcoat* interface and increases the shear strain at the *primer/metal* interface. The intensity of the equivalent elastic and shear strains however, depends critically on the local particle distribution with the effects of ΔP being confined to interfaces between the PU and particles within the local particle configuration. In the primer-only case no particle is further away from the external electrolyte than the primer thickness whereas in the primer/topcoat case regions of the primer undergoing leaching may be hundreds of microns away from the scribe. Clearly, as seen in Fig. 13 this leads to the geometric difference in that the growth of the channel network is in the plane of the primer in the primer/topcoat case, but

across the plane of the coating in the primer-only case. It may also mean that, given identical arrangements of particles, the resulting clusters may be different in the primer/topcoat case to the primer only case because the shear strain may create a different arrangement of channels, both at the Li_2CO_3/PU interface and within the PU itself.

As noted above clusters enhance the formation of channel networks since the FEA shows that strain concentrates at the inorganic particle/ PU interface and is confined to the local particle configurations. A particle in a cluster has, by definition, a nearest neighbour which is another particle in the cluster. If internal stress is confined by the neighbouring particles then the cluster is more likely to be prone to the development of a channel network. Moreover, if stress concentration is significant then the shape of the particle type may also be important. Stress concentrates on sharp edges and points on particles. The two types of particles with angular shapes are the Li_2CO_3 and $BaSO_4$ particles. If two different inorganic additives have distinct shapes for example, rounded spheres versus acicular particles, then the channel network may be more likely to develop along clusters of acicular particles [83]. In this case the high solubility of the Li_2CO_3 particles and their angular shape makes them much more susceptible to being incorporated into the developing cluster channel network.

4.4. Clusters and critical pigment volume concentration (CPVC)

Cluster formation can also be considered in the context of the CPVC. The CPVC is the point where there is not enough binder in the system to coat all the inorganic particles. The cluster model suggests that particles need to be in close proximity to each other to allow for formation of the cluster and also for release of the internal electrolyte. This means the particles have to be either in direct contact with each other or perhaps connected through the generation of microscopic channels created by internal stress. The case of direct contact would seem to contravene the CPVC rule locally (the term "locally" here means throughout the cluster but doesn't necessarily mean to a confined volume within the primer). In a past study the authors observed that the smallest separation observed between $SrCrO_4$ particles was between 50 and 100 nm [74]. But it was not clear whether this space was filled with epoxy (fulfilling the CPVC criterion) or was void (not fulfilling the CPVC criterion). Clearly, if the internal electrolyte leaches from within the primer then a connected network has been created despite the material properties of space between particles. Bierwagen et al. [84] suggested that a local PVC > CPVC could be formed when the PVC was close to the CPVC and inferred that this was a poor outcome from a paint design perspective. However, the results presented here and the previous chromate results indicate that having a PVC at or above the CPVC may be useful for the delivery of inhibitors from within the primer since it allows for leaching from deeper within the primer providing a critical concentration of inhibitor to heal corrosion damage. Thus, for high solids primers there may be a range of PVCs close to the CPVC (or above) which allows the best chance of cluster formation thereby facilitating inhibitor release.

4.5. Clusters and percolating systems

Closely related to the PVC and CPVC is the concept of the percolation threshold which has been discussed by the current authors as well as others [36,74]. These studies suggest that when any individual cluster of particles dissolves it then reaches the percolation threshold, *i.e.,* a point where all voids in the cluster provide a continuous transport network for leaching. It is important here to distinguish between percolation required for transport of Li through the channel network and a channel network for the external electrolyte to gain access to the underlying metal, these two scenarios are different. In the case of Li release, the percolation threshold is always attained since, for any cluster/channel network connected to the scribe Li release is not prevented from occurring, even as the channel network continues to grow. This means that it may be established even just by the introduction of mechanical

damage caused by scribing where the percolating network for Li leaching is only as deep as the mechanical damage. Perhaps the more important change from the perspective of Li release is the change in geometry and size of the percolating cluster with time. At the early stages, it is introduced by mechanical damage, at longer times detachment extends the channel network deeper into the primer along finer channels and at long times it may be a network comprising channels and voids where particles have completely dissolved. All three cases fulfil the percolating network criterion, but their different geometries will have quite different transport kinetics. This area is the key area for further investigation.

5. Conclusions

A range of characterisation techniques was used to examine the leaching of Li and other ions from the scribed edge of a Li_2CO_3-containing polyurethane coating underneath a topcoat. Depletion zones for Li and Mg were observed at the scribe edge. The depletion depth comprised two components including a zone of near complete depletion for Li as well as the development of a much deeper channel network. The zone related to near complete depletion was up to 25 μm. It was attributed to mechanical damage since it had the same depth as that caused by scribing. Channel network development as assessed by detachment around Li_2CO_3 particles was much deeper and penetrated at least to 260 μm after 168 h NSS. It was proposed that this deep attack is caused by internal forces related to the difference between osmotic pressure and swelling at sites of inhibitor dissolution. FEA analyses supported this model showing that equivalent elastic and shear strains concentrate at the interfaces of particles and are very dependent on local particle configurations where they concentrate at particle/PU boundaries. In terms of leaching, it was found that Li, Mg and Ba were all detected in the leachate collected from the coating. The highest release being Li followed by Mg with only low levels of Ba released. Lithium was released quickly upon immersion followed by Mg release such that the instantaneous molar ratio of Mg to Li changed significantly during the experiment from an initial value of nearly 0 to a maximum value of just over 2 at approximately the halfway point. At longer times the value decreased to about 1.2. Some Mg collected in leachate solutions was most likely from corrosion of the AA2024-T3, making it difficult to interpret Mg leaching in detail.

Author's statement

Prof. Hughes was responsible for PIXE and PIGE data analysis and SEM/EDS data interpretation, conceptualisation and writing of the paper.

Dr Visser was responsible for conceptualisation of the paper and leaching data collection and interpretation.

Dr Ranade was responsible for the FEA studies.

Dr Laird was responsible for PIXE and PIGE data collection.

Prof. Terryn contributed to conceptualisation, discussion and revision of the paper.

Prof. Mol contributed to conceptualisation, discussion and revision of the paper.

Declaration of Competing Interest

There are no conflicts of interest.

References

[1] P. Visser, H. Terryn, J.M.C. Mol, Aerospace coatings. Springer Series in Materials Science, 2016, pp. 315–372.

[2] R.G. Buchheit, A.E. Hughes, Chromate and chromate-free coatings, in: C. Moosbrugger (Ed.), Corrosion: Fundamentals, Testing and Protection, ASM International, Mterials Park, Oh, USA, 2003, pp. 720–735.

[3] O. Gharbi, et al., Chromate replacement: what does the future hold? NPJ Mater. Degrad. 2 (1) (2018) 12.

[4] K. Marcoen, et al., Compositional study of a corrosion protective layer formed by leachable lithium salts in a coating defect on AA2024-T3 aluminium alloys, Prog. Org. Coat. 119 (2018) 65–75.

[5] P. Visser, et al., Mechanism of passive layer formation on AA2024-T3 from alkaline lithium carbonate solutions in the presence of sodium chloride, J. Electrochem. Soc. 165 (2) (2018) C60–C70.

[6] A.E. Hughes, J.S. Laird, C.G. Ryan, P. Visser, H. Terryn, J.M.C. Mol, Particle characterisation and depletion of Li₂CO₃ inhibitor in a polyurethane coating, Coatings 7 (7) (2017).

[7] P. Visser, et al., Study of the formation of a protective layer in a defect from lithium-leaching organic coatings, Prog. Org. Coat. 99 (2016) 80–90.

[8] Y. Liu, et al., An investigation of the corrosion inhibitive layers generated from lithium oxalate-containing organic coating on AA2024-T3 aluminium alloy, Surf. Interface Anal. 48 (8) (2016) 798–803.

[9] Y. Liu, et al., Protective film formation on AA2024-T3 aluminum alloy by leaching of lithium carbonate from an organic coating, J. Electrochem. Soc. 163 (3) (2016) C45–C53.

[10] P. Visser, et al., The corrosion protection of AA2024-T3 aluminium alloy by leaching of lithium-containing salts from organic coatings, Faraday Discuss. 180 (2015) 511–526.

[11] S.P.V. Mahajanarn, R.G. Buchheit, Characterization of inhibitor release from Zn-Al-V10O28 (6-) hydrotalcite pigments and corrosion protection from hydrotalcite-pigmented epoxy coatings, Corrosion 64 (3) (2008) 230–240.

[12] S.P.V. Mahajanam, R.G. Buchheit, et al., Characterization of Zn-Al-V10O286-corrosion-inhibiting hydrotalcite pigments in epoxy resins, in: R.G. Buchheit (Ed.), Corrosion and Protection of Light Metal Alloys, 2004, pp. 270–282.

[13] R.G. Buchheit, H. Guan, Formation and characteristics of Al-Zn hydrotalcite coatings on galvanized steel, J. Coat. Technol. Res. 1 (4) (2004) 277–290.

[14] F. Wong, R.G. Buchheit, Utilizing the structural memory effect of layered double hydroxides for sensing water uptake in organic coatings, Prog. Org. Coat. 51 (2) (2004) 91–102.

[15] W. Zhang, R.G. Buchheit, Hydrotalcite coating formation on Al-Cu-Mg alloys from oxidizing bath chemistries, Corrosion 58 (7) (2002) 591–600.

[16] A.N. Salak, et al., Anion exchange in Zn-Al layered double hydroxides: in situ X-ray diffraction study, Chem. Phys. Lett. 495 (1–3) (2010) 73–76.

[17] S.K. Poznyak, et al., Novel inorganic host layered double hydroxides intercalated with guest organic inhibitors for anticorrosion applications, ACS Appl. Mater. Interfaces 1 (10) (2009) 2353–2362.

[18] D. Alvarez, et al., Characterization of hybrid sol-gel coatings doped with hydrotalcite-like compounds to improve corrosion resistance of AA2024-T3 alloys, Prog. Org. Coat. 68 (1–2) (2010) 91–99.

[19] J. Tedim, et al., Corrosion protection of AA2024-T3 by LDH conversion films. Analysis of SVET results, Electrochim. Acta 210 (2016) 215–224.

[20] C.S. Neves, et al., Layered double hydroxide clusters as precursors of novelmultifunctional layers: a bottom-up approach, Coatings 9 (5) (2019).

[21] A. Collazo, et al., Effect of the addition of thermally activated hydrotalcite on the protective features of sol-gel coatings applied on AA2024 aluminium alloys, Electrochim. Acta 56 (23) (2011) 7805–7814.

[22] M. Kendig, M. Hon, A hydrotalcite-like pigment containing an organic anion corrosion inhibitor, Electrochem. Solid State Lett. 8 (3) (2005) B10–B11.

[23] H.N. McMurray, G. Williams, Inhibition of filiform corrosion on organic-coated aluminium alloy by hydrotalcite-like anion-exchange pigments, Corrosion 60 (3) (2004) 219–228.

[24] G. Williams, H.N. McMurray, Inhibition of filiform corrosion on polymer coated AA2024-T3 by hydrotalcite-like pigments incorporating organic anions, Electrochem. Solid State Lett. 7 (5) (2004) B13–B15.

[25] G. Williams, H.N. McMurray, Anion-exchange inhibition of filiform corrosion on organic coated AA2024-T3 aluminum alloy by hydrotalcite-like pigments, Electrochem. Solid State Lett. 6 (3) (2003) B9–B11.

[26] S. Bohm, et al., Novel environment friendly corrosion inhibitor pigments based on naturally occurring clay minerals, Mater. Corros.-Werkstoffe Korrosion 52 (12) (2001) 896–903.

[27] J.D. Gorman, et al., Oxide formation on aluminium alloys in boiling deionised water and NaCl, CeCl3 and CrCl3 solutions, Corros. Sci. 45 (6) (2003) 1103–1124.

[28] W. Vedder, Vermilye Da, Aluminum+Water reaction, Trans. Faraday Soc. 65 (554P) (1969), p. 561-&.

[29] A.E. Hughes, T.G. Harvey, S.G. Hardin, T. Nikpour, B. Hinton, G. McAdam, A. Galassi, A. Butler, A. Stonham, S.J. Harris, C. Figgures, S. Church, D. Dixon, P. Morgan, C. Bowden, M. Ranson, A methodology for selecting chromate replacements, ATB Metall. 43 (1–2) (2003) 467–474.

[30] J.S. Laird, et al., Li leaching from Lithium carbonate-primer: an emerging perspective of transport pathway development, Prog. Org. Coat. 134 (2019) 103–118.

[31] G.M. Geise, D.R. Paul, B.D. Freeman, Fundamental water and salt transport properties of polymeric materials, Prog. Polym. Sci. 39 (1) (2014) 1–42.

[32] M.H. Shirangi, X.J. Fan, B. Michel, Mechanism of moisture diffusion, hygroscopic swelling and adhesion degradation in epoxy molding compounds, in: Proceedings - 2008 International Symposium on Microelectronics, IMAPS 2008, 2008.

[33] Y. Dong, Q. Zhou, Relationship between ion transport and the failure behavior of epoxy resin coatings, Corros. Sci. 78 (2014) 22–28.

[34] J.M. Hu, J.Q. Zhang, C.N. Cao, Determination of water uptake and diffusion of Cl-ion in epoxy primer on aluminum alloys in NaCl solution by electrochemical impedance spectroscopy, Prog. Org. Coat. 46 (2003) 273–279.

[35] J. Sinko, Challenges of chromate inhibitor pigments replacement in organic coatings, Prog. Org. Coat. 42 (3–4) (2001) 267–282.

[36] S.G.R. Emad, et al., Leaching from coatings pigmented with strontium aluminium polyphosphate inhibitor pigment- evidence for a cluster-percolation model, Prog. Org. Coat. 137 (2019) 105340.

[37] S.G.R. Emad, et al., How pigment volume concentration (PVC) and particle connectivity affect leaching of corrosion inhibitive species from coatings, Prog. Org. Coat. 134 (2019) 360–372.

[38] M. Kopeć, et al., Chromate ion transport in epoxy films: influence of BaSO4 particles, Prog. Org. Coat. 147 (2020).

[39] S. Sellaiyan, et al., Leaching properties of chromate-containing epoxy films using radiotracers, PALS and SEM, Prog. Org. Coat. 77 (1) (2014) 257–267.

[40] A.E. Hughes, et al., Revelation of intertwining organic and inorganic fractal structures in polymer coatings, Adv. Mater. (2014) p. n/a-n/a.

[41] A.E. Hughes, I.S. Cole, T.M. Muster, R.J. Varley, Combining green and self healing for a new generation of coatings for metal protection, Nat. Asia Mater. 2 (4) (2010) 143–151.

[42] A.E. Hughes, et al., Structure and transport in coatings from multiscale computed tomography of coatings - new perspectives for eelectrochemical impedance spectroscopy modeling? Electrochim. Acta 202 (2016) 243–252.

[43] F.H. Scholes, et al., Corrosion in artificial defects. I: development of corrosion, Corros. Sci. 48 (7) (2006) 1812–1826.

[44] S.A. Furman, et al., Corrosion in artificial defects. II. Chromate reactions, Corros. Sci. 48 (7) (2006) 1827–1847.

[45] Y. Peng, et al., Leaching behavior and corrosion inhibition of a rare earth carboxylate incorporated epoxy coating system, ACS Appl. Mater. Interfaces 11 (39) (2019) 36154–36168.

[46] J. Mardel, et al., The characterisation and performance of Ce(dbp)3-inhibited epoxy coatings, Prog. Org. Coat. 70 (2–3) (2011) 91–101.

[47] F. Zhang, et al., Self-healing mechanisms in smart protective coatings: a review, Corros. Sci. 144 (2018) 74–88.

[48] R.J. Santucci Jr., M.D. Holleman, J.R. Scully, Laboratory accelerated and field exposure testing of MgRP and MgORP on AA2024-T351: chemical and electrochemical protection effects, Surf. Coat. Technol. 383 (2020).

[49] J.S. Laird, et al., Particle induced gamma and X-ray emission spectroscopies of lithium based alloy coatings, Nucl. Instrum. Methods Phys. Res. B 404 (2017) 167–172.

[50] I.J. Polmear, Light Allopys: Metallurgy of the Light Metals, 3rd ed., Arnold, London, 1995.

[51] X. Zhong, et al., Multi-modal plasma focused ion beam serial section tomography of an organic paint coating, Ultramicroscopy 197 (2019) 1–10.

[52] C.G. Ryan, et al., The new CSIRO-GEMOC nuclear microprobe: first results, performance and recent applications, Nucl. Instrum. Methods Phys. Res. B 181 (1–4) (2001) 12–19.

[53] X. Wu, K. Hebert, Development of surface impurity segregation during dissolution of aluminum, J. Electrochem. Soc. 143 (1) (1996) 83–91.

[54] J.S. Laird, et al., Particle induced gamma and X-ray emission spectroscopies of lithium based alloy coatings. Nuclear Instruments and Methods in Physics Research Section B: Beam Interactions With Materials and Atoms, 2014.

[55] C. Boni, et al., Prompt gamma emission excitation functions for PIGE analysis, Nucl. Instrum. Methods Phys. Res. B 35 (1) (1988) 80–86.

[56] G.E. Dieter, Mechanical metallurgy. McGraw-Hill Series in Materials Science and Engineering, 1st ed., McGraw-Hill Book Co, London, 1988, p. 751.

[57] A. Kosari, et al., Cross-sectional characterization of the conversion layer formed on AA2024-T3 by a lithium-leaching coating, Appl. Surf. Sci. 512 (2020).

[58] N. Birbilis, et al., A closer look at constituent induced localised corrosion in Al-Cu-Mg alloys, Corros. Sci. 113 (2016) 160–171.

[59] A.E. Hughes, R. Parvizi, M. Forsyth, Microstructure and corrosion of AA2024, Corros. Rev. 33 (1–2) (2015) 1–30.

[60] R.J. Santucci Jr., et al., Scientific investigation of the corrosion performance of magnesium and magnesium oxide primers on Al alloy 2024-T351 in field exposures, Corrosion 75 (5) (2019) 440–456.

[61] D.R. Lide (Ed.), CRC Handbook of Chemistry and Physics, 71st ed., CRC Press, Boston, 1990.

[62] M. Modesti, et al., Mathematical model and experimental validation of water cluster influence upon vapour permeation through hydrophilic dense membrane, J. Memb. Sci. 229 (1–2) (2004) 211–223.

[63] D. Turan, Water vapor transport properties of polyurethane films for packaging of respiring foods, Food Eng. Rev. (2019).

[64] J.E. Huacuja-Sánchez, K. Müller, W. Possart, Water diffusion in a crosslinked polyether-based polyurethane adhesive, Int. J. Adhes. Adhes. 66 (2016) 167–175.

[65] S. Mondal, J.L. Hu, Z. Yong, Free volume and water vapor permeability of dense segmented polyurethane membrane, J. Memb. Sci. 280 (1) (2006) 427–432.

[66] M.F. Ferreira Marques, et al., Free-volume studies in polyurethane membranes by positron annihilation spectroscopy, Radiat. Phys. Chem. 68 (3–4) (2003) 573–576.

[67] J. Mähler, I. Persson, A study of the hydration of the alkali metal ions in aqueous solution, Inorg. Chem. 51 (2) (2012) 425–438.

[68] C. Vosgien Lacombre, et al., Influence of internal stresses on the physicochemical and mechanical properties evolution of pigmented epoxy systems during hygrothermal ageing, Surf. Coat. Technol. 341 (2018) 86–94.

[69] A.S. Hall, An Introduction to the Mechanics of Solids, John Wiley & Sons, Milton, 1973, p. 448.

[70] D.Y. Perera, Effect of pigmentation on organic coating characteristics, Prog. Org. Coat. 50 (4) (2004) 247–262.

[71] S.A. Furman, et al., Chromate leaching from inhibited primers - Part II: modelling of leaching, Prog. Org. Coat. 56 (1) (2006) 33–38.

[72] P. Klomjit, R.G. Buchheit, Characterization of inhibitor storage and release from commercial primers, Prog. Org. Coat. 114 (2018) 68–77.

[73] T. Prosek, D. Thierry, A model for the release of chromate from organic coatings, Prog. Org. Coat. 49 (3) (2004) 209–217.

[74] A.E. Hughes, et al., Revelation of intertwining organic and inorganic fractal structures in polymer coatings, Adv. Mater. 26 (26) (2014) 4504–4508.

[75] I.M. Zin, et al., Model electrochemical cell study of cut-edge corrosion inhibition on coil-coated steel sheet by chromate-, phosphate-, and calcium-containing pigments, J. Electrochem. Soc. 148 (8) (2001) B293–B298.

[76] F. Rezaei, et al., Evaluating water transport through high solid polyurethane coating using the EIS method, J. Coat. Technol. Res. 7 (2) (2010) 209–217.

[77] S.D. Ranade, et al., Visualizing the impact of mechanical strain and the environment on pipeline coatings from a three dimensional perspective, Prog. Org. Coat. 122 (2018) 45–55.

[78] S. Morsch, et al., Water transport in an epoxy–phenolic coating, Prog. Org. Coat. 78 (2015) 293–299.

[79] S. Morsch, et al., Mapping water uptake in organic coatings using AFM-IR, Faraday Discuss. 180 (2015) 527–542.

[80] S. Morsch, et al., Insights into epoxy network nanostructural heterogeneity using AFM-IR, ACS Appl. Mater. Interfaces 8 (1) (2016) 959–966.

[81] S. Ranade, L. Neelakantan, Exploring in situ integration of pongamia oil to improve barrier properties of polyurethane coatings, J. Appl. Polym. Sci. (2020).

[82] H.E. King, et al., Influence of inorganic solution components on lithium carbonate crystal growth, Cryst. Growth Des. 19 (12) (2019) 6994–7006.

[83] S. Ranade, M. Forsyth, M.Y.J. Tan, The initiation and propagation of coating morphological and structural defects under mechanical strain and their effects on the electrochemical behaviour of pipeline coatings, Prog. Org. Coat. 110 (2017) 62–77.

[84] R.S. Fishman, D.A. Kurtze, G.P. Bierwagen, Pigment inhomogeneity and void formation in organic coatings, Prog. Org. Coat. 21 (4) (1993) 387–403.